Bedforms and Sedimentary Features Related to Water-Depth Variations in a Sandy Tidal-Flat Environment

Yvonne Battiau, Sandra Ventalon, Romain Abraham, Vincent Sipka, Olivier Cohen, Denis Marin

Journal of Coastal Research	00	00	000–000	Charlotte, North Carolina	Month 0000

Bedforms and Sedimentary Features Related to Water-Depth Variations in a Sandy Tidal-Flat Environment

Yvonne Battiau-Queney[†]*, Sandra Ventalon[†], Romain Abraham[†], Vincent Sipka[‡], Olivier Cohen[‡], and Denis Marin[‡]

[†]Laboratoire d'Océanologie et Géosciences (CNRS)
Université de Lille
Villeneuve d'Ascq 59650, France

[‡]Laboratoire d'Océanologie et Géosciences (CNRS)
Université du Littoral-Côte d'Opale
Dunkerque 59140, France

www.cerf-jcr.org

www.JCRonline.org

ABSTRACT

Battiau-Queney, Y.; Ventalon, S.; Abraham, R.; Sipka, V.; Cohen, O., and Marin, D., 0000. Bedforms and sedimentary features related to water-depth variations in a sandy tidal-flat environment. *Journal of Coastal Research,* 00(00), 000–000. Charlotte (North Carolina), ISSN 0749-0208.

This study highlighted the variability of a wide sandy macrotidal coastal system on short timescales. Changes in water depth and exposure length were the main drivers of this variability. In the study area, the coastal system consists of three units: a lower ridge-and-runnel beach, a 1000-m-wide tidal flat, and a sandy backshore. This research is based on sedimentary features that can record physical forces, especially the bedforms at the beach surface, and their relationship with beach gradient, exposure length, and changing water depth, according to tidal, weather, and marine conditions. It also demonstrated the ability of scanning electron microscope analysis of quartz grain microtextures to indicate the level of marine and eolian energy in the coastal system. The widespread wave and current sand ripples on the tidal flat showed great variability in time and space. A minimum water depth of 0.30 to 0.50 m was required for their development. The role of wind-induced waves and the frequent interference of tidal, wave, and wind forcing mechanisms are emphasized. The development of some complex sand ripples extended over a complete lunar tidal cycle. Wind-generated sand ripples were observed only on the backshore. Their absence on the tidal flat, despite the high level of eolian energy attested by quartz microtextures, and the poor development of dunes on the backshore are explained by factors impeding eolian sand transport at the beach surface such as extreme fetch segmentation and possible shell armoring of the beach surface during dry periods. This study demonstrated the short-term variability of the beach morphology as opposed to the long-term stability of the coastal system as a whole, in which the ultradissipative tidal flat, characterized by limited sand supply, low wave energy, and high but inefficient wind energy, plays a key role.

ADDITIONAL INDEX WORDS: *Marine energy, wind energy, SEM quartz microtextures, sand ripples, wind waves, sediment supply, French North Sea coast.*

INTRODUCTION

Tidal flats are found all over the world, especially where the tidal range is large compared to the significant wave heights. In the scientific literature, the definition of tidal flats varies from author to author (Amos, 1995; Fan, 2012; Friedrichs, 2011; Jackson, 2003; Reineck and Singh, 1980). Despite the variety of definitions, there is general agreement that tidal flats share some common characteristics: a low-gradient cross-shore profile, an area consisting of unconsolidated sediments (especially sand and/or mud), and a beach surface alternately covered and uncovered by the tide, leading to large fluctuations in water depth. In the last 30 years, many publications have been produced on tidal flats. Most of them focused on hydrodynamic and morphodynamic issues and their impacts on sediment transport and deposition (Davis and Dalrymple, 2012; Desguée *et al.*, 2011; Fan, 2012; Friedrichs, 2011; Le Hir *et al.*, 2000; Malvarez, Navas, and Jackson, 2004; Wang *et al.*, 2019). They have highlighted the extreme diversity of tidal flats according to the relative importance of physical forcing mechanisms (tides, waves, and wind), biological activity, sediment supply, nearshore and offshore bathymetry, more or less sheltered position, and possible estuarine influence.

All coastal systems operate with large numbers of interacting parameters. Some of them are predictable; others depend on unpredictable short high-energy events wherein hydrodynamic and morphological effects can be decisive. In the case of tidal flats, the systems are even more complex, not only because of the very shallow water depth, which varies with the tidal cycle and the changing wave and wind forcing mechanisms, but also because of the presence of sedimentary structures, benthic fauna, and plants, which modify the roughness of the bottom. As a result, shear stresses and energy dissipation across the flats are extremely variable in space and time (Collins, 1998; Gao, 2019).

Friedrichs (2011) proposed a synthesis of tidal-flat morphodynamics using mathematical formulas to study the equilibrium shape and sediment supply to the tidal flats in response to tidal range and waves. Significantly, however, he did not consider wind as an active factor in morphodynamics and sediment transport. The review of "open coast" tidal flats by Fan (2012) emphasized the difference between mud flats and sand flats. Fan stated that "the primary forces shaping tidal flats are tidal currents and wind-induced waves" (Fan, 2012, p. 201). Modeling approaches have been widely used to study the hydrodynamics and morphodynamics of tidal flats

DOI: 10.2112/JCOASTRES-D-23-00025.1 received 23 March 2023; accepted in revision 17 July 2023; corrected proofs received 7 September 2023; published pre-print online 20 October 2023.
*Corresponding author: yvonne.battiau@orange.fr

(Friedrichs, 2011; Le Hir *et al.*, 2000; Malvarez, Navas, and Jackson, 2004; Wang *et al.*, 2019). Le Hir *et al.* (2000) proposed a numerical model that has been validated with field observations and measurements on three mud flats. They acknowledged that their model requires approximations of processes (*e.g.*, for tidal propagation) and does not account for all of these factors. Malvarez *et al.* (2004) used the modeling approach in conjunction with an empirical measurement campaign to study the morphodynamics of sandy tidal flats in Northern Ireland. The results emphasized the role of wind waves, which can be subject to strong directional changes associated with small topographic variations in the seabed. These variations also control the dissipation of wave energy due to bottom friction. Another important result was that wave-induced forces are more important than tidal currents, especially during short high-energy events. According to Malvarez *et al.* (2004, p. 744), in the "mega-dissipative" beach environments of Northern Ireland, "the tide may be regarded as a water level controller rather than a dynamic forcing factor." Desguée *et al.* (2011) carried out hydrodynamic measurements in the megatidal flat of the Mont Saint-Michel Bay (Normandy, France), which is mainly composed of fine sand and backed by salt marshes. Their preliminary results showed that sediment transport by waves is very important for the morphodynamics of the upper tidal flat, although the periods of wave efficiency are limited. However, on an annual basis, tidal currents and their associated sediment transport dominate wave processes, especially at the beginning of the high tide.

Finally, previous research on tidal flats has demonstrated the diversity of scientific approaches, which illustrates the complexity of these coastal systems and the difficulty of studying their morphodynamic and hydrodynamic characteristics. This makes it difficult to transfer the results obtained in one tidal flat to another. If the role of the wind is almost neglected in some studies, then it is considered fundamental in most others, especially through the waves it generates in shallow water.

The present study was conducted at the beach of Hemmes d'Oye, on the French North Sea coast (Figure 1). Contrary to the beach-dune systems, which are well developed along this coast and thoroughly studied (Anthony, Ruz, and Vanhée, 2009; Battiau-Queney *et al.*, 2001, 2003; Cartier and Héquette, 2013; Reichmüth and Anthony, 2008; Sedrati and Anthony, 2007; Sipka and Anthony, 1999), studies dealing with tidal flats in the region are rare (Aubry, 2010). The beach of Hemmes d'Oye has been neglected in the scientific literature, except for a few papers based on the diachronic analysis of vertical aerial photographs or LIDAR data, which attest to the great stability of the local shoreline on a multidecadal scale (Aernouts, 2005; Aubry, 2010; Chaverot, 2006; Ruz *et al.*, 2017; Zemmour, 2019). Several unpublished cross-shore profiles acquired with LIDAR between 2008 and 2020 suggest small changes in elevation on the order of a few decimeters. At the centennial scale, historical archives confirm the same trend (Briquet, 1930; Ruz *et al.*, 2017).

In the study area, a straight, 35-m-wide sand ridge lines the current upper beach limit (Figure 2). Its flat top between +9.04 and +8.60 m IGN69 (all elevation data herein refer to the French national vertical datum IGN69) and its plant communities are not typical of a coastal dune (Duhamel *et al.*, 2017). In fact, it is thought to be part of an enclosure dike built around AD 1630 with a mixture of sand, clay, peat, and straw during a period of land reclamation from the sea (Blanchard, 1906; Briquet, 1930). Its present position indicates that the shoreline has not moved significantly in the last 400 years. This long-term stability is not common along the French coast of the southern North Sea and the eastern English Channel, and it explains why this site has been neglected by most researchers, who consider it of little interest compared to other sites subject to rapid changes on multidecadal or decadal scales. However, the dual rarity of long-term stability and tidal-flat environment raises questions that this study sought to answer.

The coastal system is macrotidal. The tidal cycle has a semidiurnal periodicity. The tidal wave progresses northeastward from the eastern English Channel to the North Sea. The range of equinoctial spring tides decreases in the same direction from Somme Bay (up to 10.60 m) to the Belgian border (about 6.30 m). It reaches 6.91 m in the study area. The macrotidal environment has major morphological, hydrological, and sedimentological effects on the dynamics of the coastal system, mainly through the relative length of exposure and submergence of the different units of the coastal system and consequently the fluctuations of water depth in the intertidal zone. In this area, southwesterly winds prevail. Onshore winds are less frequent but may be associated with severe storms (Maspataud, 2011; Zemmour, 2019). In the Strait of Dover, southwesterly waves predominate (CEREMA, 2018). The modal periods of the waves vary between 5 and 7 seconds (Aubry, 2010). The height of the significant 10-year waves reaches 4.64 m off the Flemish coast (CEREMA, 2018). The height of nearshore waves is more difficult to measure and model, despite a rich scientific literature (Aagaard and Masselink, 1999; Carter, 1989; Pezerat *et al.*, 2021). Along the coast of the southern North Sea, 80% of nearshore waves are considered to be <1.20 m high, and 60% of waves are <0.60 m high (Ruz *et al.*, 2017). Direct measurements of wave height were made at the nearby beach of Hemmes de Marck. The significant wave heights were measured during several periods of 14 days in 2007 and 2008, either in calm or rough conditions, during spring or neap tide (Aubry, 2010). They varied between 1.00 and 2.60 m on the lower beach and reached a few centimeters in calm conditions and <0.30 m in rough conditions in the inner part of the tidal flat.

The general topography of the study area is presented from land to sea (Figure 1):

(1) flat and possibly submerged lowlands (between +3.87 and +4.40 m);
(2) a low, straight sand ridge;
(3) a 12- to 15-m-wide sandy backshore; and
(4) a 1500-m-wide intertidal zone divided into a 1000-m-wide flat platform (strictly speaking, the "tidal flat") and a lower beach shaped by ridges and channels (as defined by King and Williams, 1949).

Prior to this study, preliminary visits to the site revealed

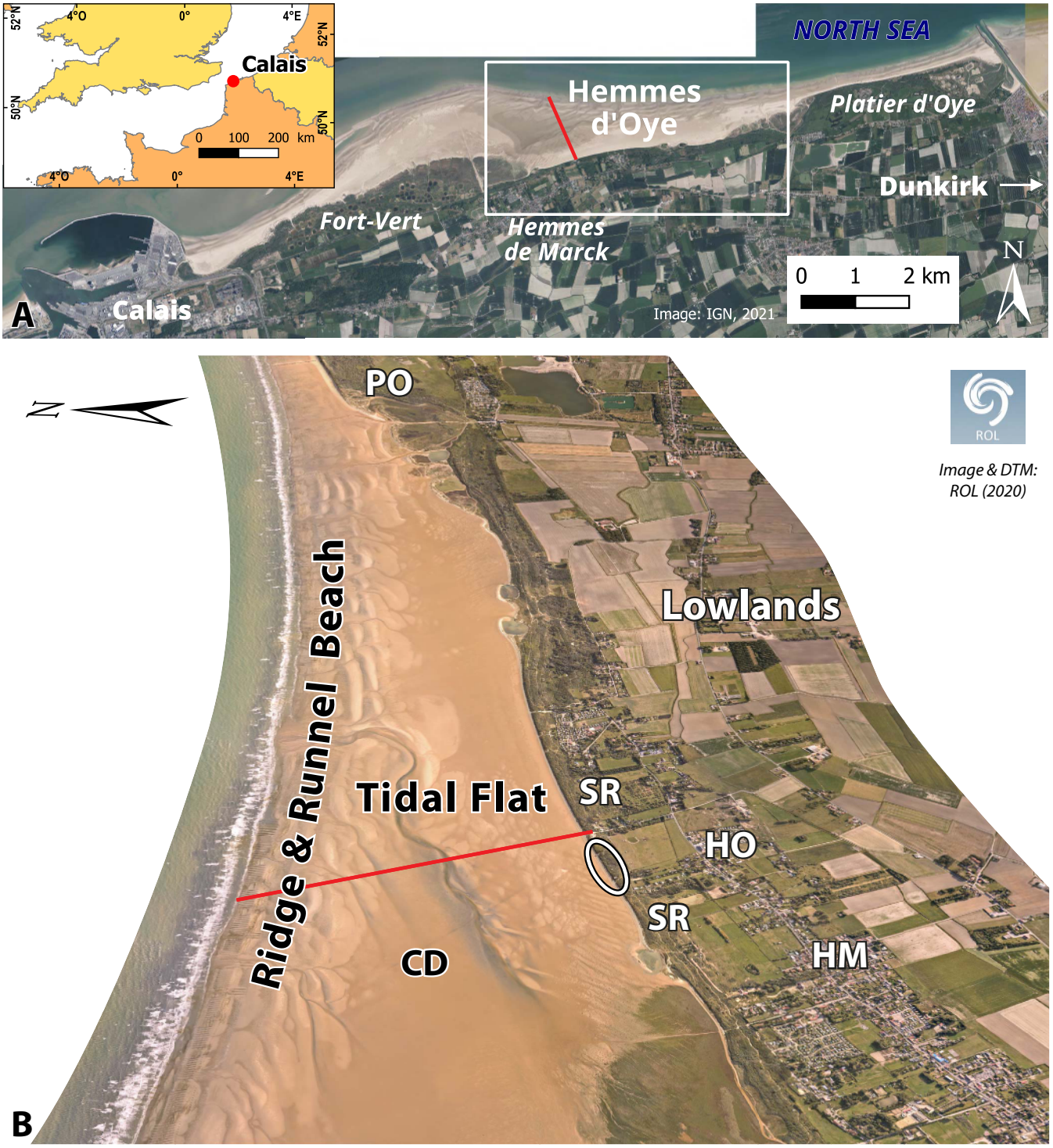

Figure 1. Study area. (A) General view (source: GEOPORTAIL, 2023). White rectangle: area of part B. (B) Textured three-dimensional (3D) model of the site (aerial photo and digital elevation model; ROLNP, 2020). R&R Beach = intertidal ridge-and-runnel beach; CD = central depression with main channel; SR = sand ridge; HO = Hemmes d'Oye. HM = Hemmes de Marck; PO = Platier d'Oye; white oval frame = location of German bunkers; red line = cross-shore profile, 10 November 2021.

that the detailed landforms can change rapidly on short timescales and are an interesting subject for research. In

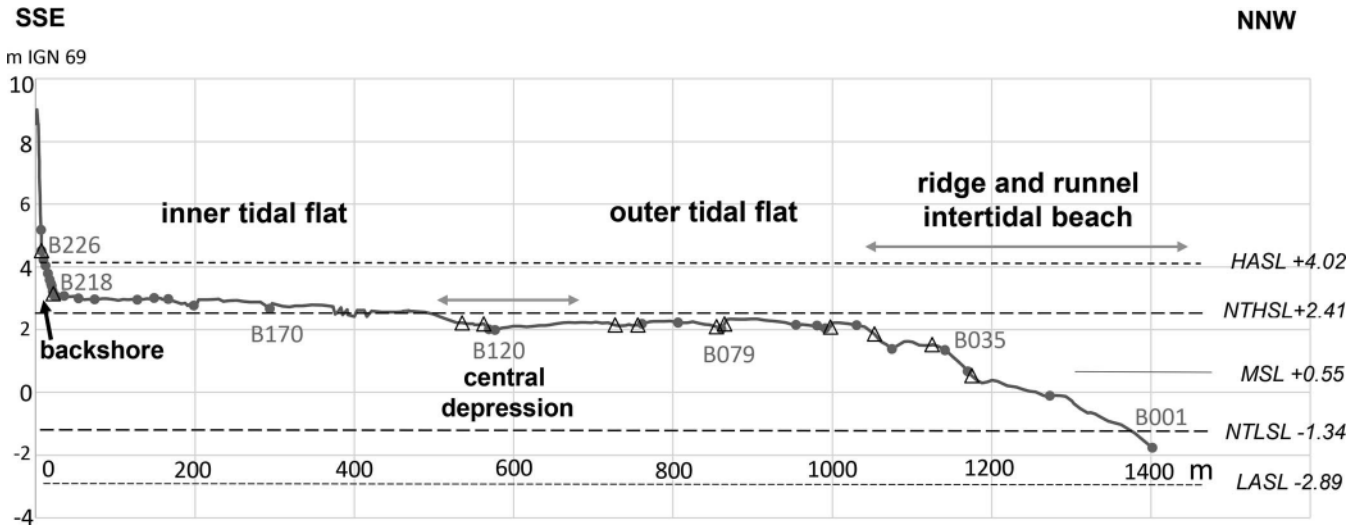

Figure 2. Cross-shore profile of the Hemmes d'Oye coastal system taken on 10 November 2021 showing the main topographic and hydro-sedimentary units: the ridge-and-runnel intertidal beach, the tidal flat, which is divided into three subunits (outer tidal flat, central depression, and inner tidal flat), and the backshore. HASL = highest astronomical sea level; NTHSL = neap tide high sea level; MSL = mean sea level; NTLSL = neap tide low sea level; LASL = lowest astronomical sea level. On the profile, gray dots indicate sampling locations, and B + numbers indicate samples analyzed by SEM.

contrast to many previous studies that aimed to model hydrodynamic and morphodynamic processes and sediment transport, the present study highlights the variability of the sandy tidal-flat environment of Hemmes d'Oye on short timescales, ranging from the tidal cycle and storm events to seasonal changes.

METHODS

A morphological and sedimentological approach was chosen to explain this variability. It was based on the working hypothesis that the effects of wave, tidal, and wind forcing mechanisms are recorded by some morphological and sedimentary features, in particular, the bedforms of the beach surface and the microtextures of the quartz grains, which form the bulk of the sediment. The study of these features, mainly based on field observations, will therefore provide information on the hydrodynamics, morphodynamics, and sediment transport in the coastal system as a function of water-depth variations and exposure time.

This study used data collected during eight field surveys from September 2021 to June 2023, under different tidal, sea, and weather conditions. First, obtaining an accurate cross-shore profile of the coastal system, from the backshore to the lowest intertidal beach, was a fundamental point at the beginning of the research. For this study, a 1400-m-long cross-shore profile of the Hemmes d'Oye beach was obtained at low tide on 10 November 2021, using a differential global navigation satellite system (GNSS) with an accuracy of ±3 cm. At the same time, along the profile, 33 samples were collected within 5 cm of the surface and georeferenced. Their locations marked any significant change in gradient, sediment texture, or bed-form structures. Thus, they well represented the environmental characteristics of the three units of the coastal system (ridge-and-runnel intertidal lower beach, tidal flat, backshore).

Particle size analysis (PSD) was performed on each sample using a Malvern Mastersizer 2000 laser diffraction instrument. Some samples collected from the inner part of the mud flat were passed through a 1.6 mm sieve to remove shell fragments that were too large for the instrument. However, the role of these shells will be discussed below. For each sample, the sorting coefficient (So) was calculated according to Folk and Ward (1957):

$$So = \frac{D84\phi - D16\phi}{4} + \frac{D95\phi - D5\phi}{6.6} \quad (1)$$

where, D is the percentile of grain size given in phi values ($\phi = -\log_2 d$, where d is the diameter in millimeters; Krumbein, 1934). In this coastal environment, the sorting coefficient is considered to be the more useful parameter, since it precisely indicates the silt content, which has significant consequences for the cohesion and response of the sediment to wave and wind forces. In order to compare the different sedimentary environments, the frequency distribution of the grain size in each sample was determined and represented on a semilogarithmic graph that combined the percentage of sediment volume (on the y axis) and the grain size in micrometers (on the x axis).

Among the samples collected, seven were selected to represent the variety of environments in terms of beach slope, water-depth variations, and length of exposure, from the lowest ridge-and-runnel intertidal beach to the base of the sand ridge. Since the sediment in the study area is mainly composed of quartz grains, the aim was to study them using a binocular microscope and scanning electron microscope (SEM). The working hypothesis was that quartz grains have recorded the complex sedimentary history in alternating

aqueous and aerial environments; surface microtextures can be identified (with backscattered or secondary electron imaging) and attributed to mechanical or chemical processes; and the chronology of marine or eolian episodes can thus be reconstructed. SEM has been widely used since the late 1960s to study the relationship between the outline and surface microtextures of quartz grains and their sedimentary history (Costa *et al*., 2013; Itamiya, Sugita, and Sugai, 2019; Krinsley and Donahue, 1968; Krinsley and Doornkamp, 1973; Le Ribault, 1977; Mahaney, 2002; Margolis, 1968; Stevic, 2015; Vos, Vandenberghe, and Elsen, 2014).

Such analyses have been performed in various environments (glacial, fluvial, eolian, marine, soils), but rarely in tidal flats. In this research, the aim was to obtain micrographs and, in some cases, to perform energy-dispersive X-ray spectroscopy (EDXS) analyses using an Environmental FEI Quanta 200 SEM coupled to a Bruker Quantax EDXS spectrometer to identify the mineralogy of some crystals. One of the most interesting aspects of these analyses was the evaluation of the changing levels of wind and marine energy in the different environments, from the wave-breaking zone of the lower beach to the backshore. The selected samples were not treated prior to analysis, as grain coatings, adherent particles, carbonates, and other minerals can provide valuable information on grain transport, deposition, and diagenesis processes. Samples were simply sieved to retain grains larger than 160 μm, which are the best candidates for microtexture analysis. In each sample, approximately 30 to 60 grains were randomly observed under a binocular microscope. Then, 10 to 15 of them were positioned on a double-sided adhesive tape on a SEM specimen holder. Although this number seems low, it is considered sufficient to investigate most of the variability within a sample (Vos, Vandenberghe, and Elsen, 2014). The specimen holder with the selected grains was then sputter coated with carbon using a Balzers SCD004 instrument. The carbon coating reduces beam penetration, produces sharper images, and minimizes electrical charging of the surface (Vos, Vandenberghe, and Elsen, 2014).

In addition to the microtextures of quartz grains, the sedimentary structures that develop on the beach surface in a tidal-flat environment are signatures of ongoing physical and biogenic processes (Amos, 1995; Reineck and Singh, 1980). Bedforms, channels, and flow patterns record the physical forces that control sediment transport and deposition on short timescales. In particular, ripples are "an expression of the organization of moving grains into morphological elements" (Amos, Kassem, and Friend, 2019, p. 1447). They can be eolian- or water-generated features. The latter are generally divided into two broad categories, either current-formed or wave-formed features, but they can also be the result of combined processes. The bedforms and other sedimentary structures on the beach surface were identified under a variety of tidal, weather, and sea conditions. Their interpretation requires consideration of meteorological and oceanographic conditions hours and days before they are observed in the field. For this purpose, data from the Calais-Marck meteorological station were used (https://www.meteociel.com). The preservation of these features depends on many factors, including the more or less cohesive nature of the sediment and the changing energy level of physical processes during tidal cycles (Davis, 2012). The duration of exposure and the water depth of each observation point during the tidal cycle were determined from data provided by SHOM, the French National Hydrographic Service (http://maree.shom.info). The reference port for this study was Gravelines.

RESULTS

The results are presented in two parts: First, the information provided by the high-resolution cross-shore profile obtained in November 2021 clearly shows the division of the coastal system of Hemmes d'Oye into three morpho-sedimentological units, differentiated by their gradient, range of water depths and duration of exposure, and also by the particle size of the beach sediment, especially the percentage of silt. Then, in each of the three units, the analysis of the sedimentary structures observed on the surface of the beach is addressed with the microtextures of the quartz grains collected in the same place. Thus, the data obtained provide valuable information on the physical and sedimentary processes in each unit.

Three Different Topographic and Hydro-Sedimentological Units

The 1400-m-long cross-shore profile recorded on 10 November 2021 was oriented SSE-NNW (Figure 1). It started at the top of the sand ridge (+8.56 m at this point) and reached the lowest beach exposed that day at −1.76 m (Figure 2). It showed an overall convex upward profile, which is common in the case of high tidal range (Dieckmann, Osterthun, and Partenscky, 1987; Kirby, 2000).

From the sea to the land, the topographic profile shows three units distinguished by their slope: a lower intertidal beach with an average slope of 1.0%, about 400 to 450 m wide; a 1000-m-wide intertidal flat platform with an average slope of less than 0.1%; and a backshore (as defined by Hesp, 1999), usually 12 to 15 m wide, with an average slope of 9.6%. The lower intertidal beach is sandy and shaped in "ridges and runnels," also called "bars and troughs" or "multiple intertidal bars" (Biausque *et al*., 2020; Kroon and Masselink, 2002). Numerous cross-shore tidal channels are another characteristic of this lower beach.

The mainly sandy intertidal platform, with elevation differences in the range of a few decimeters, is the key element of this coastal system. As it is not connected to an estuarine environment, it can be defined as an open-coast sand flat (Fan, 2012). The highest point, in its inner part, is at +3.08 m. The lowest point is at +1.99 m in a shallow central depression with a main channel, oriented SW-NE (Figure 1). At the outer edge of the tidal flat, at +2.14 m, the contact of the ridge-and-runnel beach with the tidal flat is marked by a sudden decrease in gradient. At the inner edge of the flat, the contact with the sandy backshore is even sharper, changing abruptly from 0.1% to more than 9%. Thus, this unit is very well defined in the landscape. The backshore is also well bounded landward by the base of the sand ridge, at +4.52 m, which is higher than the astronomical reference high-water level (+4.02 m at Gravelines). On 10 November 2021, with a tidal range of 4.74 m (mean tide), the high-water line was about 15 m from the sand ridge. On 27 November 2022, with a tidal

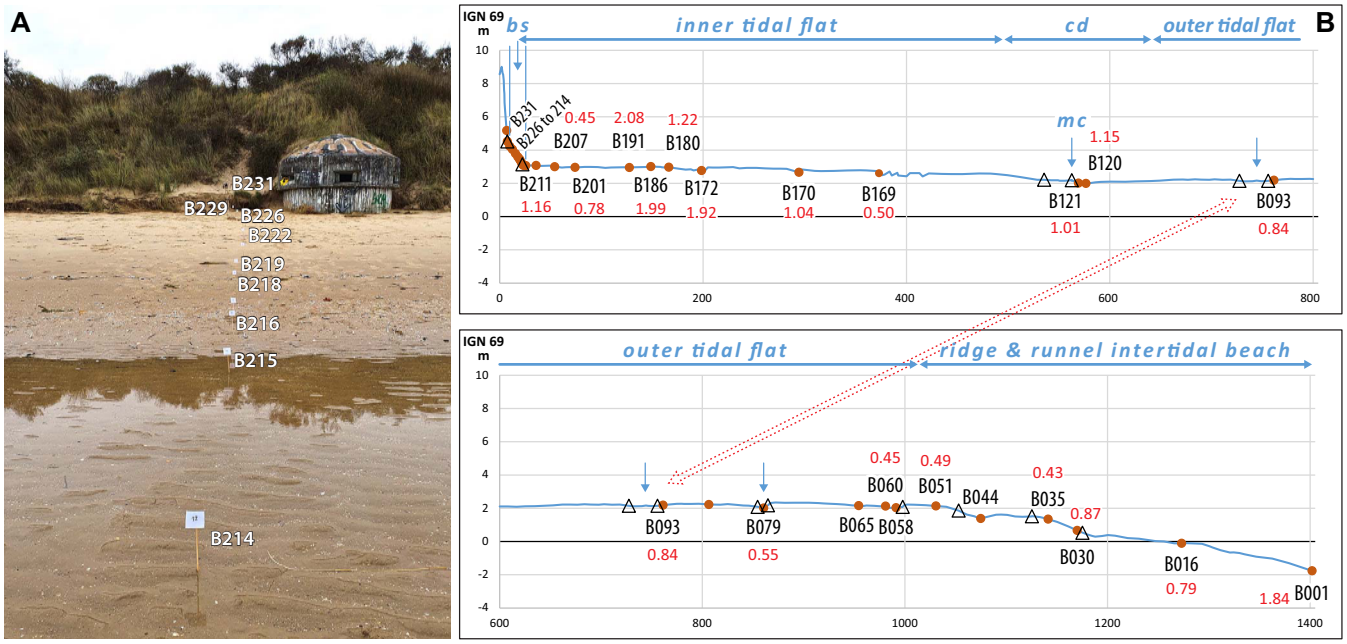

Figure 3. Location and sorting coefficient (red numbers) of samples collected on 10 November 2021. (A) Backshore and swash zone. (B) Full profile. Abbreviations: bs = backshore; cd = central depression; mc = main channel. The small vertical blue arrows indicate tidal channels.

range of 5.75 m (spring tide) and calm conditions, the high-water line was about 5 m from the sand ridge. In fact, the backshore is rarely completely inundated, except during storm surges, as was observed on 31 January 2022, with a tidal range of 5.43 m.

In the macrotidal environment of Hemmes d'Oye, the sea level varies in a range from 3.75 m (lowest neap tide) to 6.91 m (highest spring tide). On the other hand, the topography of the beach surface can be considered stable in the short term, in a range of a few decimeters. Therefore, two parameters are fundamental to understand the physical forces at work in the coastal system: the water depth and the duration of exposure. The predicted astronomical spring and neap tide sea levels were plotted on the cross-shore profile recorded on 10 November 2021 (Figure 2).

The diagram shows the division of the tidal flat into three subunits, called the "outer tidal flat" and "inner tidal flat" separated by a "central depression," which is 0.15 to 0.20 m deeper than the edges. The outer tidal flat is flooded during every tidal cycle, but with very low water depth, less than 0.40 m during neap tide, and up to 2.03 m during spring tide in calm or moderate conditions. On the other hand, a more than 450 m section of the inner tidal flat remains exposed during every neap tide cycle, while the water depth varies from less than 0.40 m to 1.50 m during the spring tide in calm or moderate conditions. The duration of exposure during a tidal cycle is a direct consequence of the variations in water depth. It exceeds 8 hours everywhere on the tidal flat, but it is limited to 3 hours in the lower part of the ridge-and-runnel beach.

The particle size analysis of the 33 samples collected along the November 2021 profile (Figure 3; Table 1) showed that particles consist mainly of quartz grains that are sand or silt in size. Almost absent on the outer tidal flat, whole or fragmented shells can be abundant on the inner tidal flat (up to 25% of the total sediment).

All samples correspond to a stock dominated by fine and medium sands. Many samples are bimodal and sometimes plurimodal (Figure 4). Silts are abundant at the base of the ridge-and-runnel beach (sample B001). They disappear on the upper part of the ridge-and-runnel beach (from B035 to B051) and are present in small quantities on the outer part of the tidal flat (B060 to B093). They are locally more abundant in the 200 m landward part of the platform (samples B172 to B191; Table 1). They are absent from the backshore. The least sorted samples (*So* above 1.20) contain 15%–25% silt. They are found at the base of the ridge-and-runnel beach and in some places on the landward part of the tidal flat. The best sorted samples are found on the backshore and the outer edge of the tidal flat. The percentage of coarse sands (>500 μm) was less than 3% in all samples.

Finally, it is difficult to find a simple logic in the results of the grain-size analysis of the 33 samples collected on 20 November 2022. To understand all the facts revealed by this analysis, it is necessary to have complementary information about the processes of transport and deposition of the sediment on the beach surface. This study used first a classical method, that is, the observation of the sedimentary structures observed in the three units defined above. However, quartz grain microtextures were also analyzed to reveal the response of the sediment to wind and marine forces in a tidal-flat environment. For better coherence and to emphasize the global characteristics of each unit, the most typical bedforms and

Table 1. *Particle size characteristics of some samples collected on 10 November 2021, including sample numbers as indicated in Figures 2 and 3, percentiles of grain size in μm (D),. sorting index (So) defined by Folk and Ward (1957), and the corresponding hydro-sedimentological unit(s).*

Sample number	D_{50} (μm)	D_{16} (μm)	D_{84} (μm)	*So*	% Silts $2 > x < 63$ μm	% Coarse Sand >500 μm	Hydro-Sedimentological Unit(s)
B001	194.45	28.04	323.48	1.84	19.95	0.82	Intertidal ridge-and-runnel beach
B016	230.88	162.11	316.86	0.79	6.25	0.15	
B030	225.00	150.50	318.16	0.87	7.16	0.21	
B035	257.09	188.73	349.54	0.43	0.00	0.63	
B051	249.42	177.13	351.99	0.49	0.00	1.35	Seaward edge of tidal flat
B060	253.12	184.54	345.11	0.45	0.00	1.00	Outer tidal flat flooded at high neap tides
B079	265.40	183.20	374.36	0.55	4.67	2.53	
B093	267.53	172.18	365.27	0.84	6.74	2.01	
B120	220.78	127.86	328.84	1.15	11.83	0.77	Main channel of the central depression
B121	239.90	155.39	341.68	1.01	9.31	1.05	
B169	237.69	166.97	334.53	0.50	2.43	0.76	Inner part of tidal flat not flooded at high neap tides
B170	223.07	137.63	331.92	1.04	8.98	1.01	
B172	152.13	20.67	283.70	1.92	24.31	0.07	
B180	227.96	142.62	328.98	1.22	10.63	0.69	
B186	178.16	21.18	322.16	1.99	23.28	1.52	
B191	170.95	16.82	325.54	2.08	26.89	1.89	
B201	243.52	176.10	325.19	0.78	6.28	0.25	
B207	251.82	182.84	348.08	0.45	0.00	1.07	
B211	252.11	182.63	336.62	1.16	0.22	0.45	
B214	270.30	194.01	374.58	0.61	1.51	2.22	
B215	242.04	147.54	358.95	1.08	9.92	2.07	Contact tidal flat/upper beach
B216	257.49	179.56	366.89	0.50	1.46	2.03	
B218	229.93	115.13	367.10	1.29	12.36	2.88	Swash zone
B219	269.64	197.94	367.65	0.43	0.00	1.55	Backshore
B222	272.19	210.77	351.25	0.36	0.00	0.49	
B226	269.72	209.07	348.94	0.36	0.00	0.47	
B229	281.08	206.66	382.87	0.43	0.00	2.40	Sand-ridge foot
B231	247.48	170.83	335.59	0.45	2.80	0.54	Sand-ridge seaward scarp

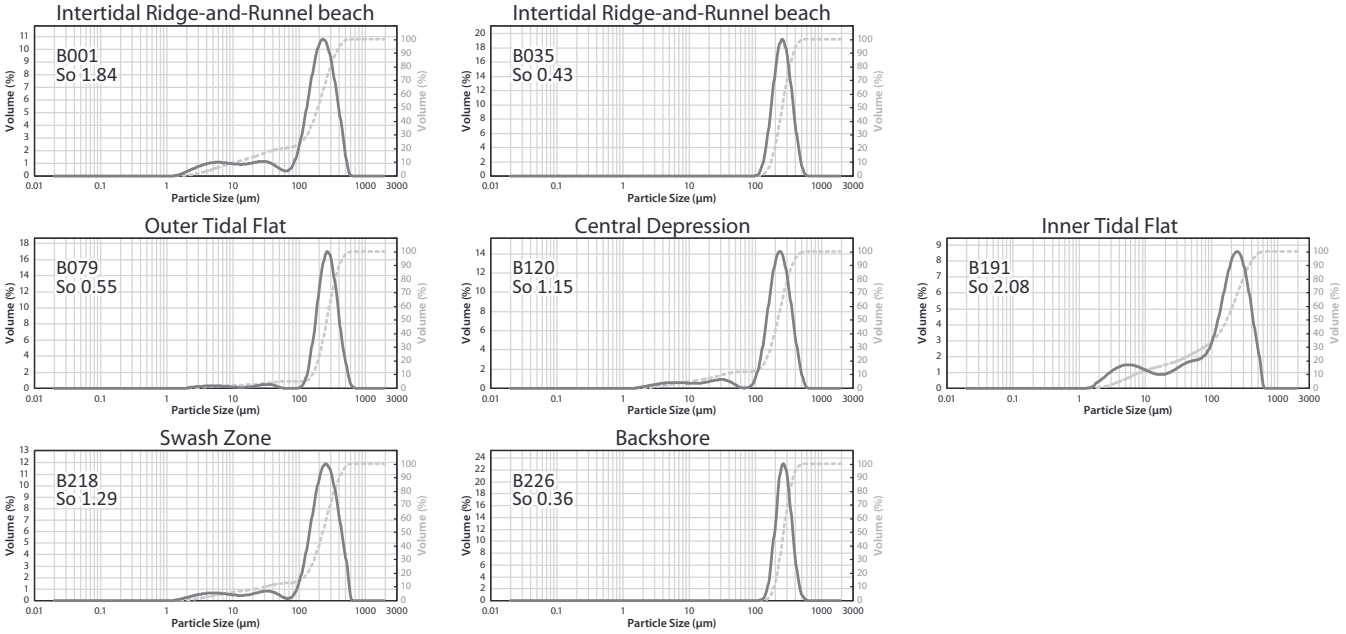

Figure 4. Frequency and cumulative curves of representative samples of the three units and subunits collected on 10 November 2021. The plots are semi-logarithmic with percent of volume on the *y* axis and grain size (μm) on the *x* axis. The number and sorting coefficient of each sample is shown (see also Figures 2 and 3). The selected samples are representative for each subunit: base and upper part of the ridge-and-runnel beach, outer tidal flat, central depression, inner tidal flat, swash zone, and backshore. In all samples, the sand grain size distribution is unimodal, with a mode between 232 and 268 μm (fine to medium sands). Clay-sized particles are absent or less than 0.4%. The percentage of silt is more variable (see Table 1), with a plurimodal grain-size distribution. Solid lines = frequency curves; dashed lines = cumulative curves.

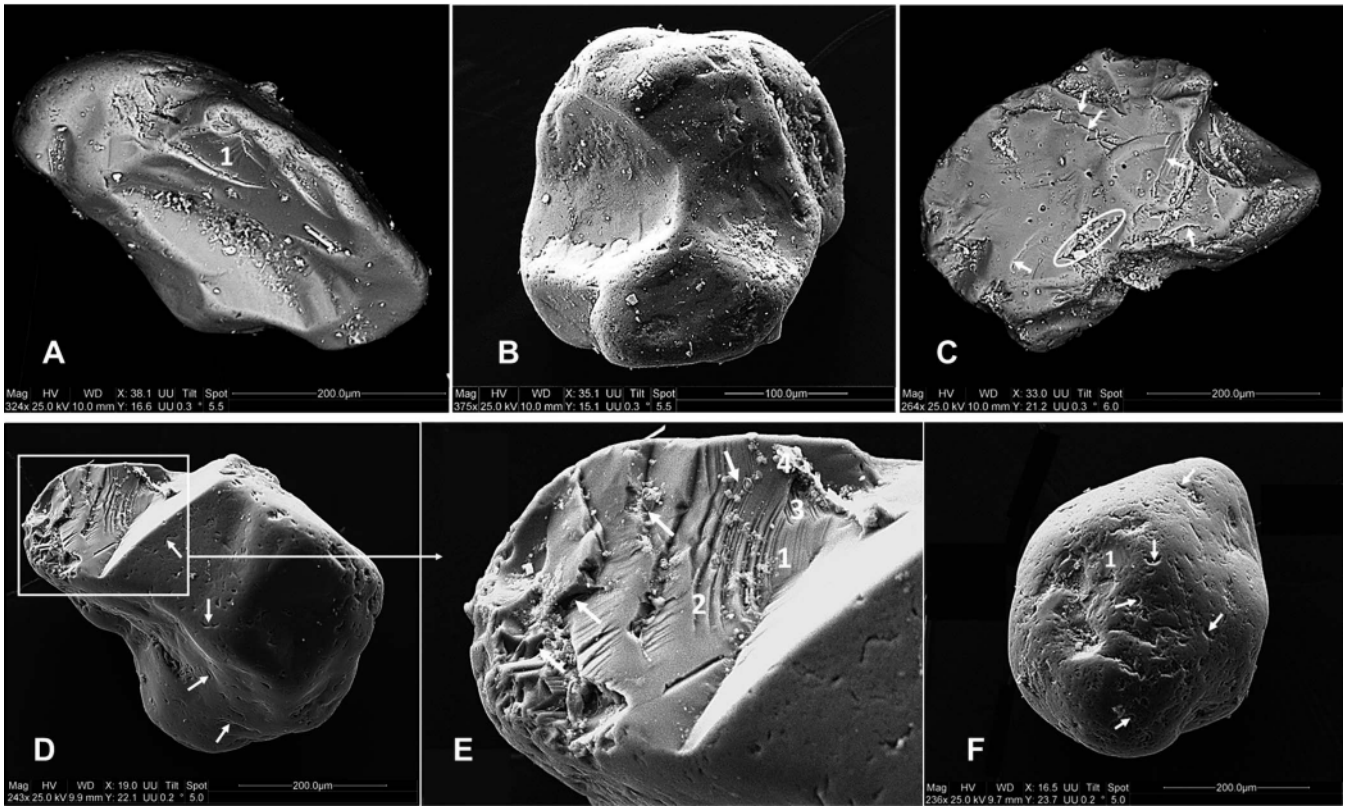

Figure 5. Microtextures of quartz grains from the ridge-and-runnel intertidal beach in samples B001 (A, B, C) and B035 (D, E, F). (A) Fresh radial features are diagnostic of violent impact (1). Silica fragments mixed with other minerals (Ca, Na, Mg, Fe, Cl) are abundant in the depressions. (B) Large conchoidal fractures are separated by thin abraded bridges. (C) Several conchoidal and radial fractures and some upturned plates (white arrows) indicate violent collisions. Silica solution microtextures are present (white oval frame). (D) Grains with subrounded contours have a shiny and polished surface, typical of marine abrasion. Many shock crescents of different orientations (arrows) are diagnostic of eolian impacts and collisions. (E) Detail of a large conchoidal fracture with sharp edges (1), indicating high impact energy. Shear marks are sometimes staircased (2 and 3). Some diatoms (arrows) and NaCl crystals (4) and many silica fragments are present in cavities. (F) A shiny grain with polished surfaces (marine abrasion) and rounded contours. Numerous shock crescents (white arrows) or cups (1) are typical of eolian impacts.

sedimentary features of each unit (or subunit for the tidal flat) are presented in turn.

Ridge-and-Runnel Intertidal Beach

This is the lowest unit of the coastal system, which is highly exposed to wave action. The average cross-shore gradient is 1%, but locally it reaches or even exceeds 2.4% (Figure 2). The water depth varies from 0 to 6.90 m, depending on the tidal range and location. At the nearby beach of Hemmes de Marck, the height of the significant incident waves was measured by Aubry (2010): At the lowest beach, this varies from less than 1.00 m in calm conditions to 2.60 m in rough conditions and equinoctial spring tide. Le Hir *et al*. (2000) estimated that the breaking point of waves is reached when H/h exceeds 0.8 (where H is the wave height, and h is the water depth). Such conditions are common on the ridge-and-runnel beach of the Hemmes d'Oye. In fact, plunging breakers are often observed even in calm conditions. This is a violent process that concentrates the dissipation of wave energy in a narrow zone (Carter, 1989).

Quartz Microtextures

The SEM analysis of the shape and microtextures of the quartz grains was carried out on two samples collected from the ridge-and-runnel beach (Figure 5): the first (B001) (Figure 5A–C) came from the lowest part of the intertidal zone, which is submerged most of the time, and the second (B035) (Figure 5D–F) was taken on a wide sand bar near the seaward edge of the tidal flat, which is exposed for 7 to 8 hours during each tidal cycle.

In all grains of sample B001, conchoidal fractures of various sizes with abraded surfaces are indicative of strong mechanical impacts in a high-energy marine environment (Krinsley and Donahue 1968; Le Ribault, 1977; Mahaney, 2002; Vos, Vandenberghe, and Elsen, 2014). Some crescent-shaped, nonoriented marks are typical of eolian impact, but these are further blunted by marine abrasion. Significant silica solution microtextures (white frame) are consistent with the short exposure time. On the other hand, grains from sample B035 indicated moderate- to high-energy marine and eolian impacts. Diatoms, NaCl crystals, quartz splinters, and siliceous spherules (silica

Figure 6. Sedimentary features and tidal channels in the ridge-and-runnel intertidal beach. (A, B, C) Zone of mussel cultivation (21 May 2021), tidal range 4.72 m. In the background, plunging breakers of waves. Swash marks are well visible in the sandy areas between the rows where patches of biodeposits could develop (C). White arrows indicate backwash currents. In B, dotted arrows indicate the direction of propagation of small wave ripples. (D, E, F) Tidal currents at low tide in the lowest zone of the intertidal beach. Part D is from 1 August 2022, tidal range = 5.04 m; E and F depict 28 October 2022, tidal range = 5.71 m. In E, the main ebb current (white arrows) interferes with secondary wind-induced eastward flows (dotted arrows). The ebb currents are locally highly turbulent (white circle at F) and encounter the runup of the waves. (G, H, I) Complex pattern of braided and meandering channels at ebb tide with point bars on concave banks and miniscarps on convex banks. G is from 1 August 2022, and H and I depict 28 October 2022. White arrows indicate the direction of flow.

precipitation) are present in the cavities. Fresh eolian microtextures and silica precipitation are consistent with prolonged exposure.

Bedforms, Sedimentary Features, and Tidal Channel Pattern

Sedimentary features on the ridge-and-runnel intertidal beach were observed under the different tidal, weather, and sea conditions that occurred between November 2021 and June 2023 (Figure 6). Just above the low spring tide, at about −2.20 m, rows of wooden poles ("*bouchots*" in French) were placed across the beach for mussel cultivation (Figure 6A–E). There, the high percentage of silt (see sample B001 in Table 1) may be partly due to biodeposition (McKindsey *et al*., 2011) (Figure 6C), a point that requires further research. On the beach surface between the rows of bouchots, swash marks are common, regardless of sea and weather conditions. Badly developed sand ripples can form on the sea side of the lowest sand bar (Figure 6B). The most characteristic features of the ridge-and-runnel intertidal beach are the tidal channels, which form a complex network that varies considerably in time and space (Figure 6G–I). This variability is the main characteristic of tidal channels (Hughes, 2012). Due to bidirectional flows, meanders and associated point bars have a more complex geometry than in fluvial channels. In both cases, however, lateral migration of meanders is a key process in the seaward transport of sand. In the mussel cultivation zone, ebb currents are concentrated along the rows of bouchots, where scour features are observed (Figure 6D), while the areas between the rows are slightly accreted. The speed of the current is at its maximum at low tide. It depends mainly on the tidal range, which determines the inundated area of the intertidal beach at high tide, and thus the volume of water to be evacuated. However, it also depends on the wind direction and

velocity: For example, on 26 January 2023, despite a high tidal range (5.91 m), the ebb currents were limited by strong onshore winds (gusts of 15 m s^{-1}), which slowed down the drainage of the tidal flat. Otherwise, ebb currents can be highly turbulent during spring tides. In detail, the hydrodynamic system of the channel network appears to be very complex, especially when approaching the swash zone, where ebb currents and wave runup meet (Figure 6F).

Tidal Flat

At the seaward edge of the tidal flat, the slope of the beach surface drops abruptly from more than 1% to less than 0.1%. The main consequence is a sudden reduction in wave height, as there is a linear relationship between maximum wave height and local water depth (Aubry, 2010; Le Hir *et al*., 2000). Le Hir *et al*. (2000) found that the significant wave height measured on the Brouage tidal flat (Oléron Island, France) did not exceed 15% of the water depth. On the outer tidal flat and central depression, the maximum predicted water depth reached 1.67 m at the highest point and 2.03 m at the lowest point. Applied to the study area, this suggests that the wave height does not exceed 0.30 m at any point on the flat, at least in calm conditions, in agreement with our own observations and with measurements taken on the nearby Hemmes de Marck beach: Aubry (2010) found a significant wave height of 0.36 m in the middle of the tidal flat during a storm event with N winds, but less than 0.20 m in calm conditions. Thus, the wave breaking point estimated by Le Hir *et al*. (2000) should not be reached in the Hemmes d'Oye tidal flat, as this would require a wave height of more than 1.00 m. Consequently, the dissipation of wave energy on the flat is mainly due to bottom friction, and not to breaking (Malvarez, Navas, and Jackson, 2004).

In the study area, the tidal flat is actually a sand flat, where silt-sized particles may be present in the central and inner parts, but they nowhere constitute the bulk of the sediment. Another characteristic of the flat is the presence of several WSW-ENE tidal channels originating from the nearby Hemmes de Marck mud flat (Figure 1) (Aubry, 2010). They are only 10 to 20 cm deep, but this is sufficient to modify the wave propagation, especially in the case of strong winds that can induce small waves.

The microtextures of the quartz grains and the sedimentary features observed on the beach surface will provide information on the processes that explain the great variability of the tidal flat in time and space.

Quartz Microtextures

Three samples were selected for SEM analysis (Figure 7) in each hydro-morphological subunit, as defined above. They represent the different marine and eolian environments in relation to the duration of exposure.

Sample B079 (Figure 7A,B) came from a secondary channel of the outer tidal flat, which is flooded at every high tide, but which has long emergence periods of 8 to 10 hours in each tidal cycle. The sorting is good. Mechanical and chemical properties of the grains indicate successive high-energy eolian and low-energy marine environments. Microtextures of silica precipitation (coalescing globules and small flowers) that are present are known to develop during emergence phases.

Sample B120 (Figure 7C,D) was collected in the main channel of the central depression. The site is flooded at each high tide and supports slightly shorter exposure times than the secondary channel, and it was observed in the field that water stagnates in the channel at low tide. Sorting is poor. Most of the grains in this sample are rounded or subrounded with bulbous edges and dull surfaces. The microstructures indicate strong eolian impacts, but some are further dulled by abrasion in water. NaCl crystals and abundant diatoms (Figure 7D) indicate low-energy marine environments. Silica solution microtextures are diagnostic of prolonged stagnation in seawater (Le Ribault, 1977; Vos, Vandenberghe, and Elsen, 2014).

Sample B170 (Figure 7E–H) was collected from the inner tidal flat, which is not flooded during neap tides. The sample is poorly sorted. The grains of this sample are homogeneous, 90% are rounded, and 10% are subrounded with bulbous edges. The microtextures record long periods of high-energy eolian impacts and shorter periods of low-energy marine environments.

The SEM analysis of the quartz grains showed that the inner tidal flat differs significantly from the outer tidal flat and the central depression by the higher eolian impact recorded by the quartz grains. For this reason, the sedimentary structures are presented first in the outer tidal flat and the central depression, where conditions of water depth and exposure are relatively similar (Figure 8), and then in the inner tidal flat, which is characterized by much longer exposure periods.

Sedimentary Features of the Outer Tidal Flat and the Central Depression

In the 150-m-wide area near the edge of the tidal flat, the beach sand is often unrippled and shows swash marks at low tide (Figure 8A). This was the case on 1 August 2022, with a maximum water depth of 1.02 m. On the other hand, ripples are common in the outer tidal flat and the central depression, but they are different types, depending on the water depth and proximity to the WSW-ENE tidal channels (Figure 1). During this study, which was conducted from September 2021 to June 2023, it was noteworthy that the bedforms observed in the field changed significantly from one visit to another, in accordance with changing tidal, wave, and wind conditions.

The main types of sand ripples that were observed fell into two categories, where the first was the most common. These are small sand ripples with an average length of about 6 to 10 cm and a height of about 1 to 2 cm (Figure 8B, C,H). The second category consists of megaripples with an average length of 0.60 to 1.20 m and a height of about 8 cm (Figure 8D–G).

Small sand ripples in the outer tidal flat are asymmetrical with straight or slightly undulatory crests and frequent bifurcations (Figure 8B). They indicate a seaward flow. Thus, they were formed when the tide was falling (ebb flow). These features are diagnostic of wave ripples in shallow water. In detail, complex shapes can be observed. At the outer tidal flat (Figure 8C), the main ripples interfere with secondary

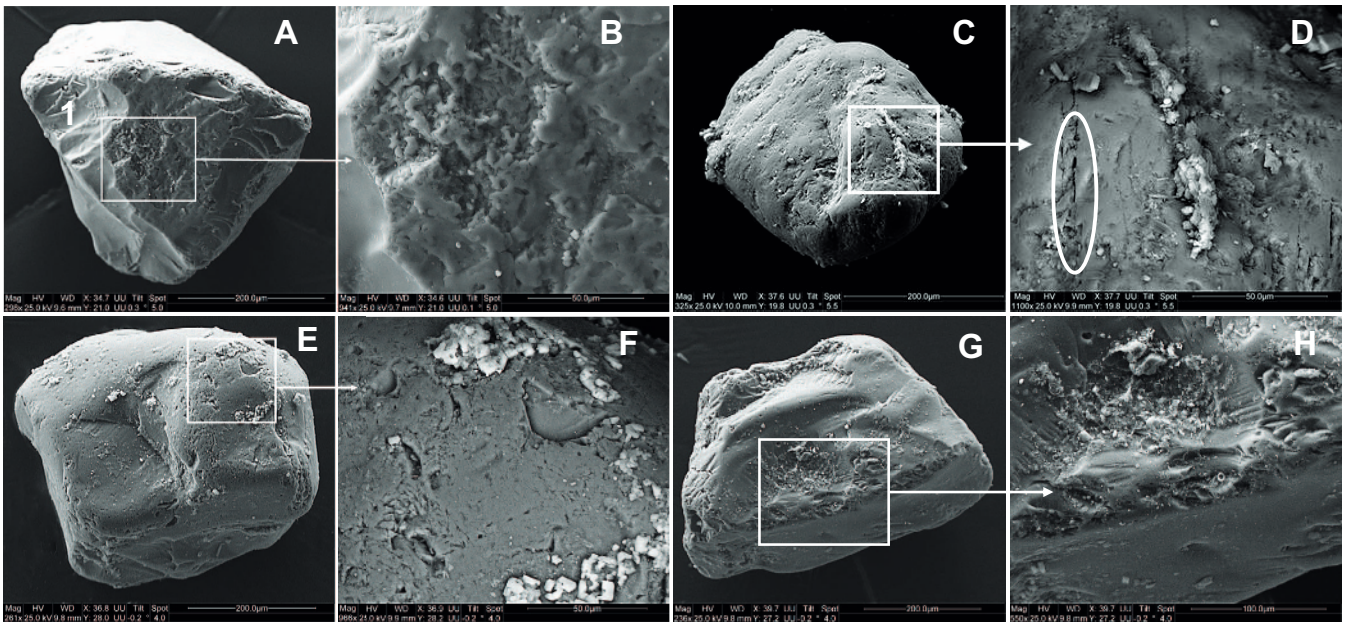

Figure 7. Microtextures of quartz grains from the tidal flat in samples B079 (A, B), B120 (C, D), and B170 (E, F, G, H). (A) The grain is subangular. Several nonoriented conchoidal fractures with sharp edges, sometimes with arcuate steps (at 1), are associated with flat cleavage surfaces. These microtextures are typical of high-energy eolian environments (Krinsley and Donahue, 1968; Vos, Vandenberghe, and Elsen, 2014). (B) The enlarged image of a detail of A shows characteristic features of silica precipitation. Diatoms are present in the cavities. (C) The grain is subrounded with numerous nonoriented crescent and V-shaped marks. (D) Detail of C showing etch pits aligned along oriented thin cracks (oval frame), which are characteristic of silica solution. Tiny silicate particles are scattered over the entire surface of the grain. (E, F, G, H) Small conchoidal factures, arcuate steps, nonoriented crescents, and V-shaped cracks diagnostic of eolian percussion and intergranular collisions. Euhedral NaCl crystals are common (F). Diatoms and features of silica precipitation are abundant in hollows (G, H).

asymmetrical miniripples in the troughs. Both ripples can form during the same tidal cycle (Reineck and Singh, 1980; Trefethen and Dow, 1960). The role of wind could be efficient to produce very small waves when the water depth decreases to a few centimeters. Double-crested ripples (Figure 8B) are common here as in many other tidal flats (Reineck and Singh, 1980). The larger ripples are formed during high tide. Then, as the water level falls, smaller waves produce smaller ripples, which are superimposed on the larger ripples.

In the central depression (Figure 8D), the small asymmetrical sand ripples are similar in size and shape, but the sediment is bimodal (Table 1, sample 120) with about 10% silt. During or immediately after the formation of the ripples at ebb tide (seaward flow, white arrow), the silt moves in suspension and preferentially settles in the troughs, where *Arenicola* traces are common.

Linguoid small sand ripples have discontinuous crests. They are less common than the previous ones and are generally associated with megaripples (Figure 8F,G). They are known to be generated at higher velocities than the small asymmetrical sand ripples described above. They therefore indicate an increase in the hydrodynamic energy of the environment (Reineck and Singh, 1980). In the field, a gradual transition from straight-crested to undulatory, and from undulatory to linguoid small ripples was observed.

Megaripples are less ubiquitous than the small ones and constitute two main types. The first category was observed only near the tidal channels of the outer tidal flat and the central depression. They are asymmetrical lunate megaripples with well-developed scour pits on their lee side (Figure 8E–G). Figure 8E is located near the tidal channel where sample B079 was collected (Figure 3). The 1.05 m pole gives the scale. The ripple length is about 1.00 to 1.20 m, and the height is about 0.15 m. On the day of the observation, the SE to SW winds were moderate (6.6 to 9.2 m s^{-1}), but strong SW gusts (14 to 20 m s^{-1}) occurred during the preceding 4 days. The maximum predicted water depth was 1.39 m, but this may have been increased by the wind. Small undulatory or linguoid asymmetrical ripples are superimposed on the stoss side of the *en echelon* lunate megaripples. This type of complex ripple was described in the Bay of Fundy by Dalrymple, Knight, and Lambiase (1978). At Hemmes d'Oye, they are only observed during spring tides. Considering that the sand size is unchanged, the main changing factors are water depth and current velocity (Reineck and Singh, 1980). Here, the asymmetry corresponds well with the strong SW winds during the 4 days preceding the observation. During spring tide, these bedforms are created by wind-induced waves that locally increase water depth and ebb current and that can create turbulent currents. Silt is not present in this area. The feature shown in Figure 8F was seen during spring tide (tidal range of

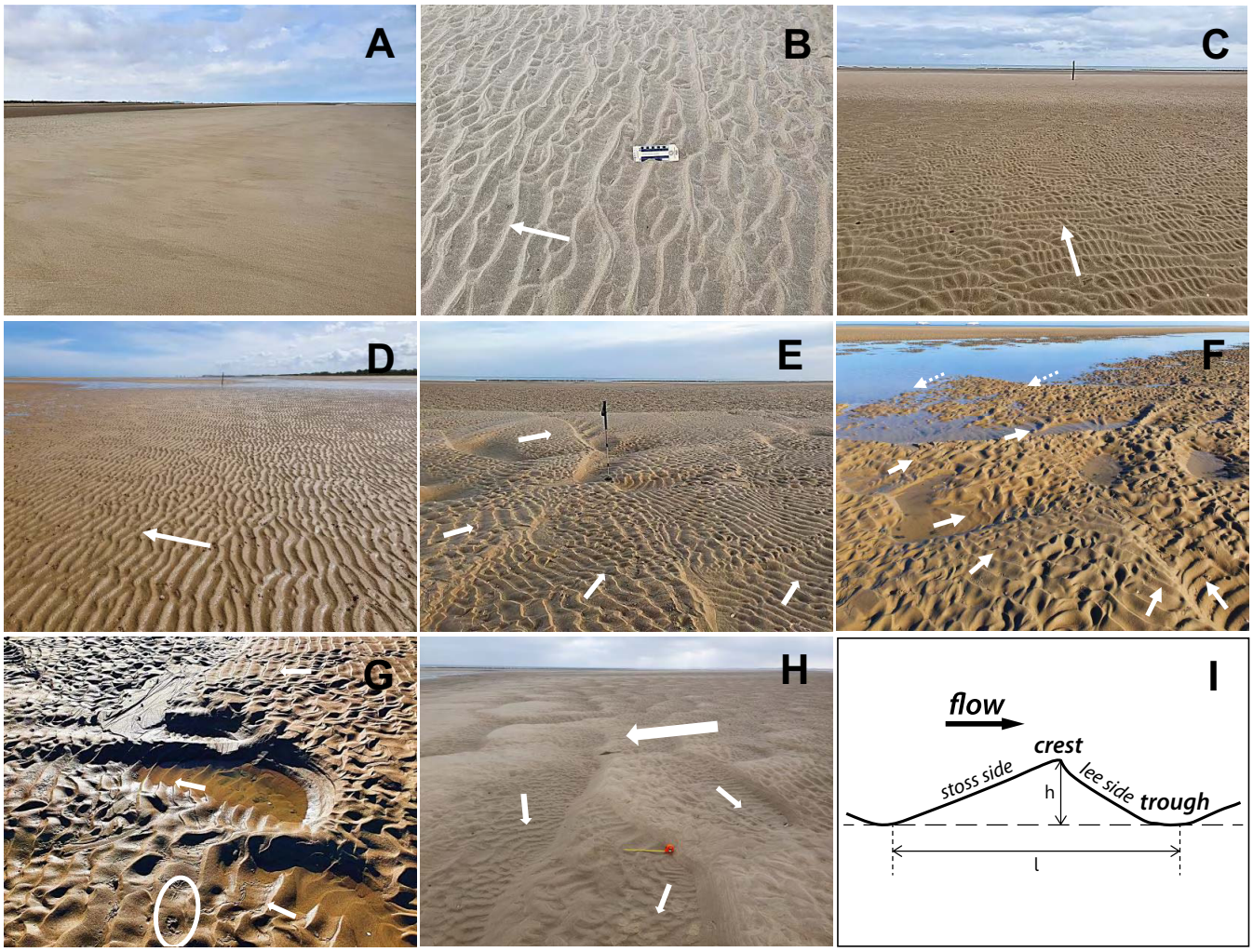

Figure 8. Sand ripples in the outer tidal flat and central depression. (A) Outer tidal flat (1 August 2022), looking west at low tide. Backwash marks are visible on the bare unrippled sandy surface. (B) Outer tidal flat (28 October 2022). Small asymmetrical sand ripples with double crests are visible. Silt is absent. (C) Outer tidal flat (1 August 2022). Interfering small asymmetrical sand ripples (seaward flow, white arrow) and miniripples in the troughs are visible. (D) Central depression (21 May 2022), looking east. Asymmetrical ripples with undulatory rounded crests and bifurcations (seaward flow, white arrow) in a silty sand are visible. (E) Outer tidal flat (28 October 2022), looking north. Small asymmetrical sand ripples are superimposed on lunate asymmetrical megaripples (white arrows indicate northeasterly flow). Silt is absent. (F) Central depression (9 October 2022) at rising tide, looking north from the southern edge of the main channel. Interfering asymmetrical lunate megaripples and small linguoid ripples with pointed crests are visible. White arrows indicate the ebb flows, which produced the ripples. Dotted arrows indicate the flood flow in the channel. (G) Same location and day as F. Detail of lunate megaripples with pointed crests and scour pits on the lee side. Small linguoid ripples are locally present. Here, the sand is silty and rich in biogenic traces (example in the oval frame). (H) Outer tidal flat (7 June 2023). Reworked lunate megaripples are visible, with flat tops and no scour pits. The large white arrow indicates their direction of migration to N. Small sand ripples (asymmetrical or linguoid) with pointed crests were produced by wind-induced waves on the day of observation (white arrows). (I) Sketch of an asymmetrical sand ripple with pointed crest. h = ripple height; l = ripple length.

5.60 m), with a light SSE breeze. The photo was taken 2 hours and 30 minutes before high tide on the south bank of the main channel of the central depression. Here, the percentage of silt is higher than in the outer flat, resulting in a more cohesive sediment, as evidenced by the abundance of biogenic activity. Although the tide was rising, the flood current in the channel was insignificant. The maximum predicted water depth that day was about 0.80 m in this area. Asymmetrical lunate megaripples with pointed crests are about 0.60 m long and a few centimeters high. Scour pits are well developed on their lee sides. The megaripples are superimposed by small asymmetrical or linguoid sand ripples with pointed crests (Figure 8G). Both types of ripples indicate a dominant NE current that occurs in the main channel at ebb tide.

The second category of lunate megaripples is rare at Hemmes d'Oye. It was observed at spring tide (tidal range of 5.51 m) in the outer tidal flat (Figure 8H). The maximum predicted water depth in this area was about 1.08 m. Light to

Figure 9. Wind action on the outer tidal flat and central depression during a gale event (30 March 2022). (A) Transport of sand grains in suspension during gusts up to 18.5 m s^{-1}. (B) Effects of winnowing of the flat sandy beach surface. (C) Effects of strong wind (direction indicated by white arrow) on small wave ripples generated by northward flows (dotted arrow).

moderate NE winds were blowing on this day and the preceding 25 days. The megaripples are about 1.00 m long and less than 10 cm high. Their *en echelon* arrangement and their shape indicate a migration to the NW. Their crests are typically flattened, and scour pits are not well developed. The lee side is covered by small asymmetrical or linguoid ripples with pointed crests indicating a flow to the SW. The small ripples are fresh and could have been formed by wind-induced waves on the day of observation or preceding days. On the other hand, the shape of the megaripples is blunt, suggesting that they formed several weeks earlier, during events of strong S or SE winds conjugated with the spring tide. This was the case only from 21 to 23 April, *i.e.* 47 days earlier. Then, they were not destroyed, but their surface was heavily reworked, more by capping of small ripples than by erosion. Such a development was described by Dalrymple, Knight, and Lambiase (1978) in the Bay of Fundy.

In all the cases described above, wind ripples were absent, in apparent contradiction to the results of the SEM analysis of the quartz grains (samples B079 and B120). Nevertheless, some short events of strong wind can occur, and the authors had the opportunity to observe one of them, on 30 March 2023 (Figure 9). The tidal range was 2.30 m (neap tide), and the area was exposed all day and the preceding day. The velocity of the WSW wind was never less than 12 m s^{-1}, with frequent gusts up to 18.5 m s^{-1}. In the outer tidal flat, silt is absent, and sand is well sorted (Table 1). During the gusts, large quantities of sand grains were transported in suspension (Figure 9A) and eventually exported to the sea. Some grains moved by saltation, but it was not possible to measure the relative importance of each mode of transport. On the other hand, field observations are useful in this case. Saltation is known to be the main process producing wind ripples (Bagnold, 1954; Sharp, 1963). Now, not only were sand ripples completely absent during the wind event, but the beach surface exhibited winnowing features (Figure 9B), which are rarely described in tidal-flat environments. These are millimeter-sized sand tongues. On the same day, south of the main channel, in an area also not flooded, the winnowing process was well visible (Figure 9C), but it was working on a rippled surface that could have formed a few days earlier at spring tide when small waves propagated northward. Here, the sediment is bimodal with about 9% silt. The ripple crests are flattened, and silt particles have settled in the troughs.

This rare, but not exceptional, event shows that high levels of eolian energy are not able to generate sand ripples when the saltation processes are less important than the transport in suspension. Bagnold (1954) already noted that ripples flatten and disappear when the wind velocity exceeds a threshold value depending on the grain size. Here, for a modal sand grain size of 240 to 260 μm, this threshold is estimated to be about 15 to 16 m s^{-1}.

Sedimentary Characteristics of the Inner Tidal Flat

The inner part of tidal flat is the area that undergoes the most pronounced changes in landscape and bedforms depending on the season and the tidal cycle. The main hydro-sedimentological characteristics are the result of long periods of exposure on a very flat surface. Stagnant seawater is omnipresent, but on surfaces that vary greatly from one event to the next.

Small sand ripples (6 to 10 cm long and less than 2 cm high) can occur anywhere, but their profile and crest geometry vary according to tidal range and weather conditions. Most are asymmetrical, indicating a landward flow. Since they were observed at low tide, it follows that the velocity of wave propagation is higher during flood tide than during backward flow, consistent with other observations in shallow water near the shore (Reineck and Singh, 1980). Here, the water depth varies from 0.00 m during neap tide to about 1.00 m when the tidal range reaches 6.20 m (high spring tide). Instantaneous field observations coupled with data on weather conditions on the same day and on previous days provided information on how the ripples formed (Figure 10).

Figure 10A: In calm conditions, the maximum water depth was about 0.65 m, and sand ripples could form on the day of observation.

Figure 10B: The site (near samples B201 and B207) was not flooded on the day of observation and for 12 preceding days. The hypothesis of wind ripples could have been considered during this long exposure period. However, the

Figure 10. Small sand ripples in the inner tidal flat. (A) 25 January 2023. Tidal range = 6.13 m. Asymmetrical ripples with straight or slightly undulatory pointed crests. Landward flow (white arrow). Silt and abundant shells are found in the troughs. Large areas of stagnant water or wet sand. (B) 1 August 2022. Calm conditions with a tidal range of 5.04 m. Small asymmetrical ripples (landward flow, white arrow) with rounded and undulatory crests and some bifurcations. Plenty of shell debris in the troughs. This is an example of wave ripples further reworked by wind action. (C) 26 January 2023, looking west. Tidal range = 5.84 m with strong NNE winds (gusts up to 13 m s^{-1}). In the foreground, there are small sand ripples with undulatory, discontinuous, flat-topped crests. Shells are abundant in the troughs. (D)(Detail from C: In the foreground, millimeter ripples are visible with convex crests oriented landward. They are superimposed on the small sand ripples. On the left, clusters of lunate ripples indicate flow to the SSW (white arrows).

longshore orientation of the crests was inconsistent with the westerly winds of the previous days. Thus, they are interpreted as wave ripples formed in very shallow water and further modified by the wind. On 19 July, with a tidal range of 5.50 m and a predicted water depth of about 0.25 m at high tide, strong westerly winds (gusting to 19 m s^{-1}) were blowing. These conditions were conducive to increasing the water depth and generating wind-induced waves that could create sand ripples at high tide. Days later, the ripples were exposed, allowing the wind to flatten their crests and concentrate shell debris in the troughs.

Figure 10C: The maximum predicted water depth in this area was about 0.50 m. Because the ripples are nearly symmetrical, the direction of flow is not clear, although some lunate-shaped ripples suggest a landward flow. In the background, the beach is still partially submerged.

Figure 10D: During the observation, NNE winds could generate very small waves that propagated landward. The wind-driven multidirectional flows were slightly turbulent despite a water depth of only 4 to 6 cm. A third type of bedforms is lunate ripples organized in clusters having variable lengths from 0.30 to 1.20 m. The handle of the shovel (12 cm) gives the scale. The pointed crests and the fresh shapes testify to the recent formation of the lunate ripples. The conditions of water depth and wind direction (NNE) and velocity were favorable for their development during the periods of high water that just preceded the observation. Thus, the bedforms in this area record a complex history with changing energy levels depending on water depth, tidal cycle, and wind regime: First, small undulatory wave ripples formed in shallow water and were further flattened by the wind when exposed; second, lunate ripples developed during a brief event of strong NNE winds that amplified the tidal flood current; third, miniripples were produced by flows induced by NNE winds at low tide in centimeter-deep puddles.

Locally observed nonrippled surfaces confirm the possible importance of wind action on the inner tidal flat as assessed by microtextures of quartz grains (sample B170). July 2022 was a dry month with several strong wind events. On 29 July and 1 August, large areas of the beach surface of the inner tidal flat were covered with shell debris (Figure 11). To assess the shell content of the sediment within 10 cm of the surface,

Figure 11. Shell armoring of the inner tidal flat and its effect on the backshore. (A) 29 July 2022, scouring of the beach surface by onshore winds (direction indicated by the white arrow). The sediment contains 15% to 25% of shells. (B) 1 August 2022, same location as A. Miniature tongues of sand result from deflation of the beach surface. (C) 1 August 2022, the backshore immediately south of A and B. A small sand ramp has formed on the windward side of the sand ridge.

the collected samples were dried, crushed, and analyzed with a Bernard calcimeter. The amount of $CaCO_3$ gives a good estimate of the shell content. It varied between 15% and 25%.

Field observations showed how deflation of a shell-rich sediment leads to armoring of the beach surface (Figure 11A,B). On 29 July and 1 August 2022, after 12 days of exposure, eolian scouring of the sand surface by onshore winds resulted in straight traces. The wind picked up grains of sand and silt, moved them in saltation or suspension, and left shell debris on the beach surface that became increasingly armored. This created a cohesive shell layer that effectively prevented the transport of underlying sand grains. Despite the difference in residual material, this process is similar to the Saharan "regs" (Cooke, Warren, and Goudie, 1993). Experiments by Cheng *et al*. (2021) explain the development of surface armoring and show that ripples cannot develop above 15%–20% shell in the sediment. On the same days, it was not surprising to observe a small sand ramp (Hesp and Short, 1999) on the seaward side of the sand ridge (Figure 11C). It was fed by the beach surface, but the small volume of the ramp resulted from the limited eolian deflation.

Nowhere and at no time did the intertidal flat of Hemmes d'Oye constitute a mud flat. The maximum percentage of fine particles rarely exceeded 25% of the beach sediment (Table 1). Contrary to many examples described in the scientific literature (Davis and Dalrymple, 2012; Fan, 2012; Reineck and Singh, 1980), there is no sediment grading from sand, near the low-water line, to mud, near the high-water line. Clay-sized particles are absent throughout. Silt particles are almost completely absent in the outer tidal flat. They are present in small quantities in the channels of the central depression. On the other hand, the presence of silt is a major feature of the inner tidal flat (Figure 12), either as patches of thin laminar veneers over rippled sand or mixed with sand in areas easily recognizable by biogenic structures and bioturbation.

An example of the first type was observed on 27 October 2022 (Figure 12A), 2 hours after high tide. The maximum water depth in this area was 0.60 to 0.70 m. In the background, the Hemmes de Marck mud flat is recognizable by its vegetation. In the foreground, a thin layer of silt that covers asymmetrical sand ripples without disturbing their pointed crests indicates a laminar flow that moved silt in suspension. Both features (the small sand ripples and the silt layer) formed during high tide, but the small sand ripples could have formed 3 days before the day of observation (spring tide), while the suspended silt particles could have settled on the day of observation.

In the western part of the study area, silt deposits tend to be thicker with frequent accumulations of millimeter-thick horizontal laminae over sand ripples (Figure 12B,C). The scouring process only affects the silty cohesive sediment, leaving the underlying sand ripples undisturbed. Thus, the energy needed to develop the feature is moderate, although it requires a turbulent current generated by wind-induced waves in shallow water. This was the case during the 3 days preceding the day of observation (tidal range of 6.06 m and water depth of 0.60 m on 7 November). Further east, especially in a 200- to 300-m-wide strip close to the backshore, silt is mixed with sand (Table 1, samples B172 to B191). Abundant biogenic structures and bioturbation characterize the sediment (Figure 12D).

Finally, the bedforms of the tidal flat confirm the low or very low level of marine energy, as evidenced by quartz microtextures. When the tide rises on the flat platform, the seawater propagates in a laminar flow that can transport silt in suspension but does not disturb sand ripples (Figure 13). According to field observations, when the water depth reaches 0.30 to 0.50 m, small waves can be generated by the flood current (landward flow), even in calm conditions, allowing the development of 6- to 10-cm-long sand ripples. Less frequently, megaripples and scour marks can form in and near the tidal channels when the wind increases the velocity of the current, especially during ebb tide. On the other hand, when the wind velocity exceeds 15 to 16 m s^{-1}, the sand grains move in suspension rather than by saltation and can no longer develop small ripples. The other aspects of wind effects will be considered in the discussion.

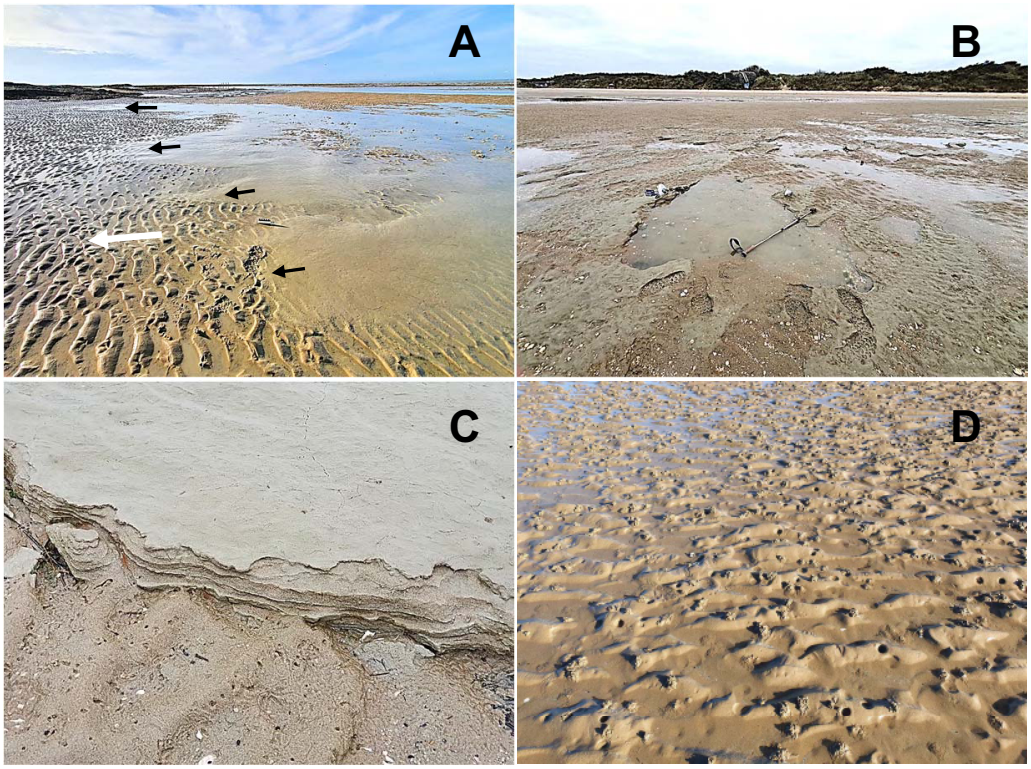

Figure 12. Silt deposits in the inner tidal flat. (A) 27 October 2022, looking WNW towards the mud flat of Hemmes de Marck. Spring tide (tidal range = 5.75 m) under calm conditions. Small asymmetrical sand ripples (landward flow, white arrow) are covered by a thin layer of silt that has advanced from the NW (black arrows). (B, C) 10 November 2021, tidal range = 4.74 m, calm conditions. Deposition of thin horizontal silt laminae over sand ripples. At B, several scour pools developed into silt deposits. (D) 9 October 2022, tidal range = 5.60 m, calm conditions. Biogenic structures in a silty sand, especially fecal mounds and feeding pits of *Arenicola marina*. The sand ripples have been disturbed by bioturbation.

Backshore

As mentioned above, the contact between the tidal flat and the backshore is marked by a sudden slope break from 0.1% to 9.6% (Figure 2). The position of the high-water line varies with the tidal range. In calm conditions, the sea does not reach the slope break when the tidal range is less than 5.20 m. For example, on 29 July 2022, with a tidal range of 4.79 m, the high-water line was 46 m from the base of the sand ridge (Figure 14). On a photo taken 1 hour and 30 minutes after high tide (Figure 14A), it was well identified by a strip of wet gray silt, while just above it, desiccation cracks could be seen on dry silt that could not have been deposited after 19 July, at the end of the previous spring cycle, when the tidal range reached 5.52 m. When the sea reaches the slope break, the hydrodynamic response depends on the wave energy. In most cases, the breaking point is not reached because the wave height is too low (Figure 14B). This was the case on 27 October 2022 with a tidal range of 5.75 m (spring tide). On the other hand, on 31 January 2022, with a moderate tidal range of 5.43 m and strong NW winds (gusts of 19 m s^{-1}), the backshore was completely inundated up to the base of the sand ridge, and weak spilling breakers could form (Figure 14C). Thus, the morphology of the backshore and the swash zone varies greatly in time, depending on the tidal range but also on the wind conditions. Both parameters determine the amount of energy recorded by the quartz grains microtextures.

Quartz Microtextures

Two representative samples were taken (Figure 15): B226 (Figure 15A) came from a site that is exceptionally flooded; B218 (Figure 15B,C) was located in the swash zone, which is flooded for less than 2 hours when the tidal range exceeds 5.5 m. The sorting of B226 is very good (Table 1). All grains are rounded. The general shape and microtextures are typical of eolian quartz: nonoriented crescents, V-shaped cracks, and small conchoidal fractures. There is no evidence of aqueous impact. Sample B218 is poorly sorted. Most grains are rounded; the remainder are subrounded. All grains show typical eolian microtextures: fresh crescent marks, percussion pits, and nonoriented small fresh conchoidal fractures. However, in contrast to the purely eolian grains of B226, the abraded surfaces and the common presence of euhedral NaCl crystals on all grains of sample B218 are consistent with short periods of low-energy marine environment.

Bedforms and Sedimentary Features

Most of the time, there is a sharp juxtaposition of wave sand ripples on the tidal flat and shelly debris that forms a small

Figure 13. Laminar flow as the sea advances over the tidal flat. 8 October 2022, tidal range = 5.23 m. The small sand ripples are not disturbed by the landward flow.

berm in the swash zone (Figure 16). This was the case on 21 May 2022, after 4 days of spring tide (Figure 16A). The backshore was not flooded on the day of observation and the preceding day. The 6- to 10-cm-long sand ripples of the tidal flat have flat-topped undulatory crests. Rill marks on some crests indicate that they were reworked at low tide in very shallow and calm water. On the same day (Figure 16B), cusp and horn swash marks were well identified in the shell deposit. They were formed during the previous days. A graded cross-shore distribution was observed, where the coarsest shell particles settled to the bottom, while lighter shell debris moved up and down with alternating runup and backwash currents. Direct observations of the swash process in calm or moderate conditions showed that the up and down currents easily move shells but are generally unable to move quartz grains, indicating a very low level of wave energy. On 27 October 2022 (Figure 16C), the tidal range was 5.75 m under calm conditions. Here, the shell berm is separated from the rippled flat by a narrow silty strip rich in *Peringia ulvae* crawl tracks. The ripples are asymmetrical (landward current) with straight crests and rill marks on the stoss faces. They were formed in the days before when small waves were generated by onshore winds, but the other bedforms are typical of a very low level of marine energy.

The sharp boundary between rippled and nonrippled surfaces (Figure 16), at the contact between the inner tidal flat and the swash zone, provides an opportunity to evaluate the minimum water depth required for ripple development. The contact is located at about +3.08 m, where the water depth

Figure 14. Incident waves on the backshore for different tidal range and wind conditions. (A) 29 July 2022, the high-water line (white arrow) is 46 m from the base of the sand ridge. Desiccation cracks have formed in the dry silt (oval frame). (B) 27 October 2022, spring tide. Waves propagate and reach the backshore without breaking. (C) 31 January 2022. Strong onshore winds can produce weak spilling breakers.

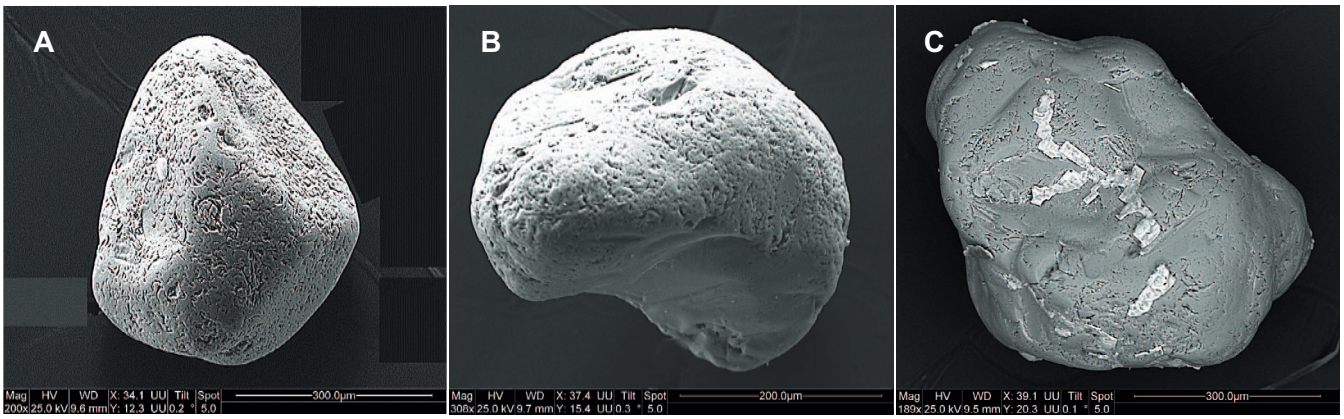

Figure 15. Microtextures of quartz grains from the backshore. (A) Sample B226, taken near the base of the sand ridge. The grain is rounded with typical eolian microtextures and lacks any aqueous impact. (B, C) Sample B218 collected in the swash zone. Grains are rounded with fresh eolian microtextures that interfere with features produced in a low-energy marine environment (abraded surfaces and euhedral NaCl crystals).

varies from 0.05 m at mean tide (tidal range about 5.00 m) to 0.84 m at equinoctial spring tide (tidal range 6.91 m). Ripples disappear on the steeper slope of the swash zone, where the water depth decreases abruptly. Thus, 0.30 to 0.50 m seems to be the minimum water depth to consider. This explains why sand ripples are widespread in the central depression, quite common on the outer flat, where the predictable tidal range is close to 4.50 m, but less common on the inner flat, where a minimum tidal range of 5.50 m is required in calm conditions.

The upper beach is the only part of the Hemmes d'Oye coastal system where wind ripples and some true eolian dunes can be observed, but they are rare and ephemeral (Figure 17). Small shadow dunes indicate longshore transport to the east (Figure 17A). Sand ramps may be deposited at the base of the sand ridge when sand deflation is active on the tidal flat (Figure 17B). The pioneer vegetation (especially *Cakile maritima*, *Euphorbia paralias*, *Elytrigia juncea*, *Leymus arenarius*) plays an important role in sand trapping (Figure 17C). However, all these dunes can be eroded or even destroyed when the sea and wind conditions allow the waves to reach the sand ridge (Figure 17D).

DISCUSSION

The main theme of the present study is the variability of the Hemmes d'Oye coastal system on short timescales. Thus, the bedforms and other sedimentary features were observed in the field from September 2021 to June 2023 under different tidal, marine, and weather conditions. They were also addressed by analyzing the microtextures of the quartz grains, which form the bulk of the sediment of the coastal system and provide information on the sedimentary history in aqueous or aerial environments. Finally, the analysis of the wave, tidal, and wind forcing mechanisms in the coastal system through the bedforms showed that the topographic division into three units also corresponds to three different hydrosedimentological units. Two main parameters have to be

Figure 16. Bedforms of the swash zone. (A) 21 May 2022, tidal range = 4.72, looking east. Sharp contact between asymmetrical flat-topped sand ripples and a shell berm. (B) Same day. Swash marks (regular distribution of cusps and horns) are well visible in the shell deposit. (C) 27 October 2022, view looking west, 2 hours after high spring tide. Standing water is visible in a narrow silty strip with abundant tracks of *Peringia ulvae*, at the contact between fresh asymmetrical sand ripples (landward flow) and the shell berm. Rill marks have formed on the stoss side of the sand ripples.

Figure 17. Eolian dunes on the backshore. (A) 8 October 2022, tidal range = 5.23 m, calm conditions, W or SW winds. Wind ripples and shadow dunes. (B) 6 June 2023, tidal range = 5.48 m. A fresh onshore breeze has been blowing all week. A sand ramp has formed at the base of the sand ridge, fed by deflation on the tidal flat. (C) 27 October 2022, tidal range = 5.75 m, calm conditions. Pioneer vegetation on the upper backshore. (D) 10 November 2021, tidal range = 4.74 m, after the spring tides of the previous 3 days (tidal range = 6.06 m on 7 November with westerly winds). A 50- to 60-cm-high sand cliff has cut through an eolian deposit.

considered: the length of exposure of the beach surface and the water depth when it is flooded. Both parameters interact and depend on the predictable tidal periodicity, but also on the unpredictable wind conditions.

Ridge-and-Runnel Intertidal Beach

This type of beach is common along the English Channel coast, but it is rarely associated with a tidal-flat environment. At Hemmes d'Oye, the 400- to 450-m-wide lower intertidal beach is highly exposed to wave breakers and to strong ebb currents in the cross-shore tidal channels. This results in a high level of wave and current energy, as evidenced by the quartz microtextures, which contributes to the movement of large quantities of sand, either seaward or landward, depending on the tidal periodicity. Field observations have shown that it is important to consider the direction and velocity of the winds, as they can enhance or slow the currents. The ridge-and-runnel intertidal beach appears to be an area of intense sand exchange with the subtidal zone: export by the tidal channels when the tide is out and import by the incoming waves when they break in plunging. Previous studies along the northern French coast have highlighted the primary role of subtidal nearshore banks in supplying sand to coastal systems (Aernouts, 2005; Aubry, 2010; Corbau, 1995; Garlan, 1990; Héquette *et al.*, 2009; Latapy *et al.*, 2020; Tessier *et al.*, 1999). They form a huge sedimentary reservoir wherein onshore and longshore migration has been demonstrated. It is important to note that the subtidal sandbanks are very close to the coast from Calais to Hemmes de Marck, but they are more distant from Hemmes d'Oye. From this point of view, the coastal area of Hemmes de Marck, just to the west, is better supplied with sand than the study area. Further research is needed to evaluate the amount of sediment imported to the lower intertidal beach and exported to the subtidal zone.

On the contrary, the import of sand from the ridge-and-runnel beach to the tidal flat seems to be limited or even insignificant. The main reason is the abrupt loss of energy when the waves reach the edge of the tidal flat. It was noted that the distinct microtextures of the quartz of the ridge-and-runnel beach, in particular, the marks of strong mechanical impacts in a high-energy marine environment (Figure 5), are not found on the outer tidal flat (Figure 7). However, they should be preserved on some grains if there was a regular supply of sand from the ridge-and-runnel beach. The export of sand from the tidal flat to the lower beach has not been studied in detail, but it has been observed that the ebb currents in the channels draining the outer flat are negligible most of the time and are unable to produce well-developed sand ripples. Thus, the seaward edge of the tidal flat appears to be a natural boundary between two hydrodynamic units that exchange very little sediment. Further research is needed to investigate this point in more detail, but a working hypothesis is that the supply of sand from the lower beach to the tidal flat is very poor.

Tidal Flat

The present study has shown the extreme variability of bedforms within a few centimeters of the platform surface. This is the expression of a very complex hydro- and morphosedimentary system in which numerous factors interact, some of which are completely unpredictable.

Wave Sand Ripples

Water-formed sand ripples are widespread on the tidal flat. They result from the interaction between the near-bed flows and the evolving bed roughness. The mechanisms that generate these small-scale rhythmic bedforms from the "chaos of sediment transport" (Amos, Kassem, and Friend, 2019, p. 1448) by current, wave, or combined wave-current flows have been intensively studied since Bagnold (1946) (Amos, Kassem, and Friend, 2019; Reineck and Singh, 1980; Trefethen and Dow, 1960). In previous studies of sand ripples, it is generally accepted that they form under turbulent flow conditions. Field observations in the study area showed that a turbulent regime can develop in a few centimeters of water as long as the wind velocity reaches 13 m s^{-1} (Figure 10C,D). Thus, it is important to consider not only the predictable water depth and length of exposure as a function of tidal range, but also the unpredictable wind climate and possible sea-level surges. There is little research on the relationship between water depth and sand-ripple development. However, field observations at Hemmes d'Oye showed that the

variation of water depth in space and time is a fundamental parameter. As mentioned above, a water depth of 0.30 to 0.50 m seems to be necessary to develop 6- to 10-cm-long sand ripples. This research has also shown that wind ripples cannot form when the wind speed exceeds 15 to 16 m s^{-1}, a threshold that favors the transport of sand grains in suspension.

This study confirmed the importance of wind-induced waves in the development of bedforms on the tidal flat. Previous research has shown that they can undergo sharp changes in direction due to refraction and diffraction associated with slight variations in the topography of the seabed (Malvarez, Navas, and Jackson, 2004). This was indeed observed in the study area. In the inner part of the tidal flat, the meter-sized puddles provide a miniature laboratory to test theoretical hypotheses, such as: Very small wind waves could generate millimeter-scale ripples (Figure 10D). This research showed that small sand ripples can be preserved for several days and even over an entire neap-spring cycle. As mentioned earlier, on the inner part of the flat, asymmetrical sand ripples generally indicate landward flow, regardless of wind direction. They form at rising tide as a result of interfering wave and current mechanisms. Their good preservation at low tide confirms previous research on tidal flats showing the higher energy level of flood flows compared to ebb flows (Trefethen and Dow, 1960). However, field observations at the backshore–tidal flat interface show that this energy asymmetry does not result in net onshore sediment transport, as is often assumed in other tidal flats (Desguée *et al*., 2011; Fan, 2012; Le Hir *et al*., 2000).

Wind Action on the Tidal Flat

In addition to waves generated by wind in shallow water, this study highlighted the complex role of wind in a macrotidal coastal system. Given the high levels of wind energy indicated by the quartz microtextures, one would expect to see significant deflation of sand grains on the long-exposed surfaces of the tidal flat and massive transport of sand either in the direction of the prevailing westerly winds or landward in the case of onshore winds. Obviously, this is not the case. There are no wind ripples on the tidal flat, and dune development on the backshore is very poor. Several features of the coastal system explain why eolian sand transport is severely impeded. First, the actual fetch on the tidal flat is limited by the moisture content of the sand and the presence of multiple puddles of seawater that persist at low tide (Figures 10 and 12). It is known that the troughs of macrotidal ridge-and-runnel beaches impede eolian sand transport by segmenting the fetch (Vanhée, Anthony, and Ruz, 2002). According to experimental studies carried out on the Clipon beach (Dunkirk), where the grain size is similar to the sand of Hemmes d'Oye, wet sand requires a wind velocity of 11 m s^{-1} to initiate sand transport (Tresca, 2013). Such velocities are not uncommon at Hemmes d'Oye. However, at Hemmes d'Oye, fetch segmentation is particularly advanced due to the presence of multiple puddles and shallow channels with standing water, the effects of which on wind deflation could be much greater than a regular system of bars and troughs. Second, another factor has been highlighted in the study area, namely, the possible surface armoring of the inner tidal flat by whole or fragmented shells during dry periods (Figure 11).

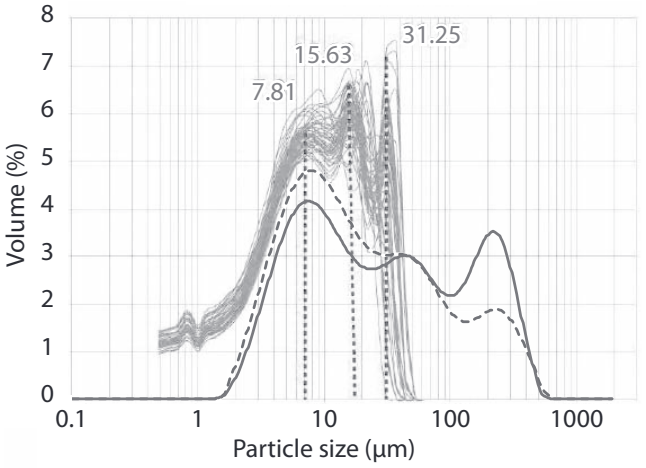

Figure 18. Frequency curves of sediments from the Hemmes de Marck mud flat compared to silt layers from the inner tidal flat of Hemmes d'Oye. Thin gray lines = Hemmes de Marck sediments. Solid and dashed lines = silt layers of Hemmes d'Oye.

Silt Deposits

Silt deposits are absent from the outer flat but are common in the central depression and the inner tidal flat. Unlike sand grains, silt particles are easily transported in water when the flat platform is flooded. They move in suspension in either turbulent or laminar flows. In the first case, when asymmetrical ripples form in silty sand, a vortex cloud of suspended silt can develop on the lee side of the ripple (Hardisty, 1994; Inman, 1957), and silt particles tend to settle in the troughs (Figure 12D). In the second case, thin layers of silt spread over undisturbed sand ripples (Figure 12A). However, as mentioned above, the silt deposits at Hemmes d'Oye are never sufficient to form a mud flat. They move here and there, settling and disappearing according to the currents active at the surface of the beach. Thus, the central depression and the inner tidal flat can be defined as an area of transit, and not as an area of accumulation of silt particles. The explanation is probably related to the lack of silt coming directly from the sea *via* the ridge-and-runnel beach. Two facts prove that the silt in these deposits comes from the mud flat of Hemmes de Marck: first, the relationship of the silt laminae and veneer to the tidal channels originating in the mud flat (Figure 1); second, the particle size of the silt laminae, which has similarities with that of samples collected in the mud flat of Hemmes de Marck (Aubry, 2010). The dominant mode at ~7.80 μm that is found at Hemmes d'Oye is also an important one at Hemmes de Marck (Figure 18).

Further east, especially in a 200- to 300-m-wide strip close to the backshore, silt is mixed with sand (Table 1, samples B172 to B191). Abundant biogenic structures and bioturbation characterize the sediment (Figure 12D). It is interesting to note that the particle size analysis indicated a mode of silt particles around 5 to 6 μm, which is smaller than in the

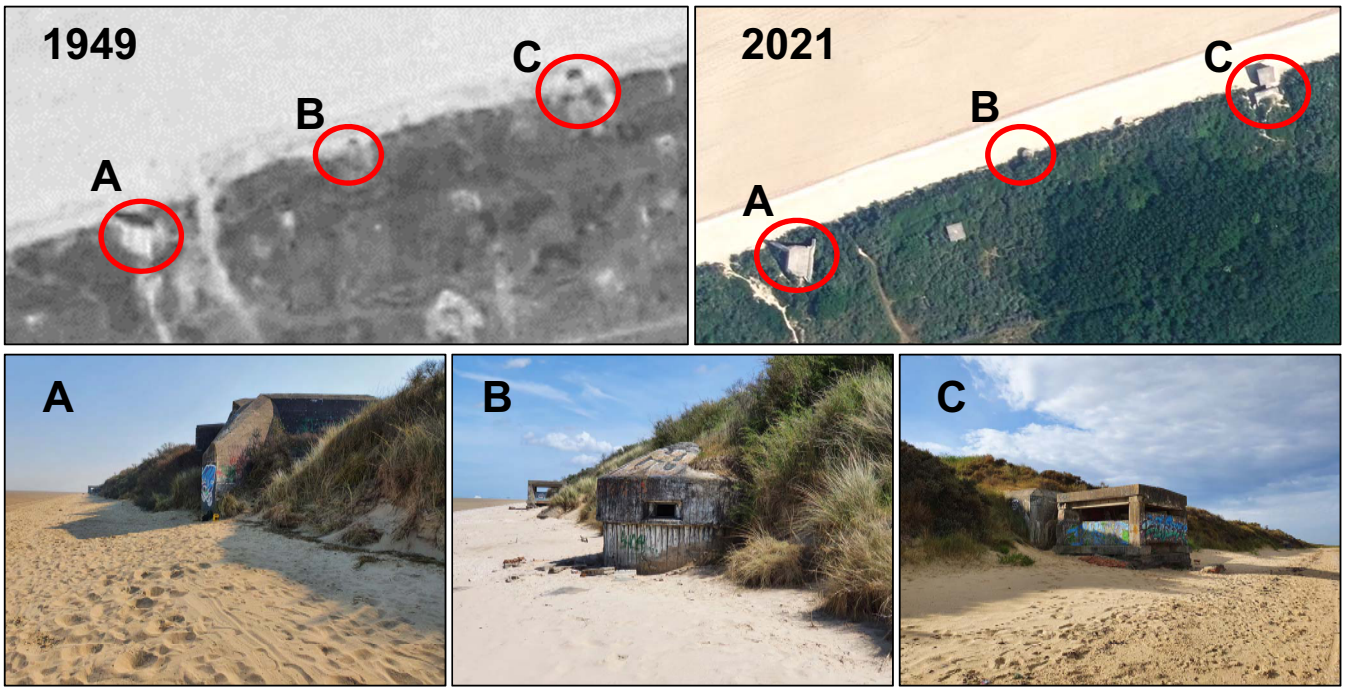

Figure 19. Stability of the upper beach of Hemmes d'Oye from 1949 to 2021. It is testified by the three bunkers of the Atlantic Wall (A, B, C), which were built in 1943/1944. The photos below (September 2021) show their good state of preservation and their position unchanged since 1949. (A) Large casemate for a 75 mm gun. (B) Conical turret for machine guns. (C) Observation tower with a shelter-bunker at the rear. Source of aerial photos: Géoportail (2023)

laminar deposits. This suggests a different origin, possibly related to quartz disaggregation by salt weathering.

Effectively, the SEM analysis revealed that the tidal flat appears to be an efficient natural system for producing silt particles. This results from the repeated alternation of emergence and flooding phases. During low tide, the seawater trapped in the fissures of the quartz grains evaporates, allowing the growth of euhedral crystals of NaCl. The crystals are then dissolved again during high tide. The rapid and repeated volume changes due to salt growth and subsequent salt solution widen the cracks and facilitate further fracturing of the quartz grains by mechanical marine and eolian impacts. This process of "salt weathering" (or "haloclasty") is known to produce silt from quartz disaggregation (Cooke, Warren, and Goudie, 1993; Goudie, Cooke, and Doornkamp, 1979), but it has never been described in a tidal flat. The frequent presence of euhedral NaCl crystals and tiny silica fragments scattered on the surface of the grains (Figure 7D,F), but especially their abundance near the salt crystals, suggests the importance of this mechanism, which may be an additional, although minor, source of silt on the tidal flat.

Backshore and Inner Swash Zone

Quartz microtextures show that the backshore combines high levels of eolian energy with low or very low levels of marine energy (Figure 15). Here, the wind is a potentially active transport agent. When it blows from the west, it has a long potential fetch and can move dry sand on the narrow backshore, provided it has sufficient velocity (Bauer and Davidson-Arnott, 2002; Friedrichs, 2011; Jackson and Cooper, 1999). In the study area, field measurements and observations indicated that the threshold velocity to initiate sand movement is approximately 7 m s^{-1} for the local particle size (Aubry, 2010). The result is eastward longshore sand transport that can initiate small shadow dunes (Figure 17A), but without significant accumulation (Arens, 1994; Ruz and Meur-Férec, 2004). Weather conditions that combine strong onshore winds with a brief event of high evaporation rate are rare but possible. In this case, sand accumulation on the backshore can change the morphology of the upper beach within a few hours. In the study area, it does not take the form of classical incipient foredunes; instead, small sand ramps develop on the seaward side of the sand ridge (Figure 17B).

The other fundamental characteristic of the swash zone at the contact of the backshore with the tidal flat is the low or very low level of marine energy at all times, even during storm events. This is evidenced by the microtextures of the quartz grains, but also by some morphological features, including a small berm composed entirely of light shell fragments or a narrow strip of silt rich in undisturbed biogenic traces (Figure 16). This is consistent with the remarkable morphological stability of the upper backshore, as evidenced by the unchanged position of the base of the sand ridge since the end of World War II (Figure 19). The low level of wave energy on the backshore has an important consequence: Because the sand ridge is not subject to serious erosion, the

lowlands, which are below the highest sea level at the rear (Figure 1), have never been inundated, even during the most severe storms that have been recorded in the southern North Sea, *e.g*., in February 1953, February 1990, and November 2007 (Maspataud, 2011).

CONCLUSIONS

Many features of the Hemmes d'Oye coastal system can be found in other tidal flats around the world. However, the combination of all of them is specific to this location. Here, the 1000-m-wide flat sandy platform appears to be an almost autonomous area with very little sediment exchange with the other two units. It has all the characteristics of an ultradissipative environment (Kroon and Masselink, 2002; Short, 1999; Wright and Short, 1984). Sediment mobility on the tidal flat is significantly hindered by several natural features, and the potential for marine erosion is very low when the sea reaches the backshore.

The present study emphasized the critical role of water depth variations on wave and wind forcing mechanisms and consequently on the physical processes that are constantly changing in time and space. These variations depend on the predictable tidal range, but also on unpredictable weather and marine factors. It is therefore very difficult to model this type of coastal system. This research demonstrates the usefulness of an approach based on field observations of sedimentary features. The applicability of SEM analyses of quartz microtextures has also been demonstrated by the additional information they provided on the magnitude of wave and wind energy in this type of coastal system.

The role of wind was emphasized to explain the variety of bedforms due to wind-induced waves, which can generate turbulent flows sufficient to develop widespread small sand ripples and less frequent megaripples. On the other hand, several other characteristics, identified by sedimentary features observed in the field, tend to strongly impede sand transport by wind, despite the high eolian energy evidenced by quartz microtextures. During dry periods, which are theoretically the most favorable conditions for eolian deflation, shell armoring of the beach surface or cohesive layers of silt effectively protect the underlying sand grains from movement.

A paradoxical characteristic of the Hemmes d'Oye coastal system is the contrast between the extreme variability of surface landforms on short timescales and the remarkable stability of the overall morphology on long timescales. In the context of the present study, a working hypothesis is that this long-term stability implies a sediment balance resulting from inefficient hydrodynamic mechanisms in a zone of limited sand supply and sediment mobility and low or very low wave and tidal current energy on the 1000-m-wide tidal flat. Further research will investigate this hypothesis.

ACKNOWLEDGMENTS

This research was supported by the Centre National de la Recherche Scientifique (CNRS), the University of Lille, and the University of Littoral-Côte d'Opale through funds allocated to the Laboratory of Oceanology and Geosciences (UMR 8187). The authors are grateful to four anonymous reviewers for their constructive comments, which helped to significantly improve the manuscript. They would also like to acknowledge the thorough and helpful review of the text by the editor.

LITERATURE CITED

Aagaard, T. and Masselink, G., 1999. The surf zone. *In:* Short, A.D. (ed.), *Handbook of Beach and Shoreface Morphodynamics*. Chichester, U.K.: Wiley, pp. 72–118.

Aernouts, D., 2005. Le rôle des changements bathymétriques à l'avant-côte sur l'évolution des littoraux meubles du Cap Gris-Nez à Dunkerque, Côte d'Opale, Nord de la France. Dunkerque, France: Université du Littoral-Côte d'Opale, Thèse de doctorat, 196p. + annexes (published online, HAL).

Amos, C.L., 1995. Siliciclastic tidal flats. *In:* Perillo G.M.E. (ed.), Geomorphology and Sedimentology of Estuaries. Amsterdam, The Netherlands: Elsevier, *Advancement in Sedimentology 53*, pp. 273–306.

Amos, C.L.; Kassem, H., and Friend, P.L., 2019. Ripple marks. *In:* Finkl, C.W. and Makowski, C. (eds.), *Encyclopedia of Coastal Science*. Cham, Switzerland: Springer, pp. 1447–1454. doi:10.1007/978-3-319-48657-4_262-2

Anthony, E.J.; Ruz, M.H., and Vanhée, S., 2009. Aeolian sand transport over complex intertidal bar-trough beach topography. *Geomorphology*, 105(1–2), 95–105.

Arens, S.M., 1994. Aeolian Processes in the Dutch Foredunes. Amsterdam, The Netherlands: University of Amsterdam, Ph.D. thesis, 150p.

Aubry, A., 2010. Processus hydrodynamiques et bilans morphosédimentaires d'un littoral macrotidal en accrétion: Etude in situ et par télédétection spatiale. Application aux Hemmes de Marck, Nord Pas de Calais, France. Dunkerque, France: Université du Littoral-Côte d'Opale, Thèse de doctorat, 333p. (published online, HAL).

Bagnold, R.A., 1946. Motion of waves in shallow water. Interaction between waves and sand bottoms. *Proceedings of the Royal Society* (London), A187(1008), 1–18. https://doi.org/10.1098/rspa.1946.0062

Bagnold, R.A., 1954. *The Physics of Blown Sand and Desert Dunes*. London: Methuen, 265p.

Battiau-Queney, Y.; Billet, J.-F.; Chaverot, S., and Lanoy-Ratel, P., 2003. Recent shoreline mobility and geomorphologic evolution of macrotidal sandy beaches in the north of France. *Marine Geology*, 194(1–2), 31–45.

Battiau-Queney, Y.; Fauchois, J.; Deboudt, P., and Lanoy-Ratel, P., 2001. Beach-dune systems in a macrotidal environment along the northern French coast (English Channel and southern North Sea). *In:* Healy, T. (ed.), *International Coastal Symposium (ICS 2000): Challenges for the 21st Century in Coastal Sciences, Engineering and Environment*. *Journal of Coastal Research*, Special Issue No. 34, pp. 580–592.

Bauer, B.O. and Davidson-Arnott, R.G.D., 2002. A general framework for modeling sediment supply to coastal dunes including wind angle, beach geometry, and fetch effects. *Geomorphology*, 49(1–2), 89–108.

Biausque, M.; Grottoli, E.; Jackson, D.W.T., and Cooper, J.A.G., 2020. Multiple intertidal bars on beaches: A review. *Earth-Science Reviews*, 210, article 103358.

Blanchard, R., 1906. *La Flandre. Etude géographique de la plaine flamande en France, Belgique et Hollande*. Paris: Armand Colin, 530p.

Briquet, A., 1930. *Le littoral du Nord de la France et son évolution morphologique*. Paris: Armand Colin, 439p.

Carter, R.W.G., 1989. *Coastal Environments. An Introduction to the Physical, Ecological and Cultural Systems of Coastlines*. London: Academic, 617p.

Cartier, A. and Héquette, A., 2013. The influence of intertidal bar-trough morphology on sediment transport on macrotidal beaches, northern France. *Zeitschrift für Geomorphologie*, 57(3), 325–347. doi:10.1127/0372-8854/2013/0105

CEREMA (Centre for Studies and Expertise on Risks, the Environment, Mobility and Urban Planning) (collator), 2018. *Dynamiques et évolution du littoral—Fascicule 1. Synthèse des*

connaissances de la frontière belge à la pointe du Hourdel. Bron, France: CEREMA, 499p.
Chaverot, S., 2006. Impact des variations récentes des conditions météo-marines sur les littoraux meubles du Nord-Pas-de-Calais. Dunkerque, France: Université du Littoral-Côte d'Opale, Thèse de doctorat, 266p.
Cheng, C.H.; de Smit, J.C.; Fivash, G.S.; Hulscher, S.J.M.H.; Borsje, B.W., and Soetaert, K., 2021. Sediment shell-content diminishes current-driven sand ripple development and migration. *Earth Surface Dynamics*, 9(5), 1335–1346, doi:10.5194/esurf-9-1335-2021, 2021.
Collins, M.B., 1998. Tidally-induced flow structure over intertidal flats. *Estuarine, Coastal and Shelf Science*, 46, 233–250.
Cooke, R.; Warren, A., and Goudie, A., 1993. *Desert Geomorphology*. London: University College London Press, 526p. doi:10.1201/b12557
Corbau, C., 1995. Dynamique sédimentaire en domaine macrotidal: Exemple du littoral du Nord de la France (Dunkerque). Lille, France: Université Lille-USTL, Thèse de doctorat, 233 p. (published online, HAL).
Costa, P.J.M.; Andrade, C.; Mahaney, W.C.; Marques da Silva, F.; Freire, P.; Freitas, M.C.; Janardo, C.; Oliveira, M.A.; Silva, T., and Lopes, V., 2013. Aeolian microtextures in silica spheres induced in a wind tunnel experiment: Comparison with aeolian quartz. *Geomorphology*, 180–181, 120–129.
Dalrymple, R.W.; Knight, R.J., and Lambiase, J.J., 1978. Bed forms and their hydraulic stability relationships in a tidal environment, Bay of Fundy, Canada. *Nature*, 275, 100–104.
Davis, R.A., Jr., 2012. Tidal signatures and their preservation potential in stratigraphic sequences. *In:* Davis, R.A., Jr., and Dalrymple, R.W. (eds.), *Principles of Tidal Sedimentology*. Dordrecht, The Netherlands: Springer, pp. 34–55.
Davis, R.A., Jr., and Dalrymple R.W. (eds.), 2012. *Principles of Tidal Sedimentology*. Dordrecht, The Netherlands: Springer, 622p. doi:10.1007/978-94-007-0123-6_3
Desguée, R.; Robin, N.; Gluard, L.; Monfort, O.; Anthony, E.J., and Levoy, F., 2011. Contribution of hydrodynamic conditions during shallow water stages to the sediment balance on a tidal flat: Mont-Saint-Michel Bay, Normandy, France. *Estuarine, Coastal and Shelf Science*, 94(4), 343–354.
Dieckmann, R.M.; Osterthun, M., and Partenscky, H.W., 1987. Influence of water-level elevation and tidal range on the sedimentation in a German tidal flat area. *Progress in Oceanography*, 18, 151–166.
Duhamel, F.; Farvacques, C.; Blondel, C.; Delplanque, S.; Catteau, E.; Gelez, W.; Francois, R.; Prey, T.; Cholet, J.; Buchet, J., and Massard, O., 2017. *Guide des végétations littorales du Nord-Ouest de la France*. Bailleul, France: Centre régional de phytosociologie agréé Conservatoire botanique national de Bailleul, 704p.
Fan, D., 2012. Open-coast tidal flats. *In:* Davis, R.A., Jr., and Dalrymple, R.W. (eds.), *Principles of Tidal Sedimentology*. Dordrecht, The Netherlands: Springer, pp. 187–229. doi:10.1007/978-94-007-0123-6_9
Folk, R. and Ward, W., 1957. Brazos River Bar: A study in the significance of grain size parameters. *Journal of Sedimentary Petrology*, 27, 3–26.
Friedrichs, C.T., 2011. Tidal flat morphodynamics: A synthesis. *In*: Flemming, B.W. and Hansom, J.D. (eds.), *Treatise on Estuarine and Coastal Science: Sedimentology and Geology*. Amsterdam, The Netherlands: Elsevier, pp. 137–170. doi:10.1016/B978-0-12-374711-2.00307-7
Gao, S., 2019. Geomorphology and sedimentology of tidal flats. *In:* Perillo, G.M.E.; Wolanski, E.; Cahoon, D.R., and Hopkinson, C.S. (eds.), *Coastal wetlands: An ecosystem integrated approach*, *2nd edition*. Amsterdam: Elsevier, pp. 295–316.
Garlan, T., 1990. L'apport des levés bathymétriques pour la connaissance de la dynamique sédimentaire. L'exemple des Ridens de la rade aux abords de Calais. *Proceedings of Eurocoast Symposium Littoral '90* (Marseille, France, Eurocoast Association), pp. 71–75.
Géoportail, 2023. *Le portail national de la connaissance du territoire mis en œuvre par l'IGN*. https://www.geoportail.gouv.fr
Google Earth, 2023. *Google Earth*. https://earth.google.com
Goudie, A.S.; Cooke, R.U., and Doornkamp, J.C., 1979. The formation of silt from quartz dune sand by salt-weathering processes in deserts. *Journal of Arid Environments*, 22, 102–112.
HAL, 2023. French Ph.D. theses published online. https://hal.archives-ouvertes.fr
Hardisty, J., 1994. Beach and nearshore sediment transport. *In:* Pye, K. (ed.), *Sediment Transport and Depositional Processes*. Oxford, U.K.: Blackwell Scientific Publications, pp. 219–255.
Héquette, A.; Ruz, M.H.; Maspataud, A., and Sipka, V., 2009. Effects of nearshore sand bank and associated channel on beach hydrodynamics: Implications for beach and shoreline evolution. *In:* da Silva, C.P. (ed.), *Proceedings of the 10th International Coastal Symposium ICS2009*. *Journal of Coastal Research*, Special Issue No. 56, pp. 59–63.
Hesp, P.A., 1999. The beach and backshore and beyond. *In:* Short, A.D. (ed.). *Handbook of Beach and Shoreface Morphodynamics*. Chichester, U.K.: Wiley, pp. 145–169.
Hesp, P.A. and Short, A.D., 1999. Barrier morphodynamics. *In:* Short, A.D. (ed.). *Handbook of Beach and Shoreface Morphodynamics*. Chichester, U.K.: Wiley, pp. 307–333.
Hughes, Z.J., 2012. Tidal channels on tidal flats and marshes. *In:* Davis, R.A., Jr., and Dalrymple, R.W. (eds.), *Principles of Tidal Sedimentology*. Dordrecht, The Netherlands: Springer, pp. 269–300. doi:10.1007/978-94-007-0123-6_11
Inman, D.L., 1957. *Wave Generated Ripples in Nearshore Sands*. Kitty Hawk, North Carolina: U.S. Army Corps of Engineers, Beach Erosion Board, *Technical Memo*, 100p.
Itamiya, H.; Sugita, R., and Sugai, T., 2019. Analysis of the surface microtextures and morphologies of beach quartz grains in Japan and implications for provenance research. *Progress in Earth and Planetary Science*, 6, 43. doi:10.1186/s40645-019-0287-9
Jackson, D.W.T., and Cooper, J.A.G. 1999. Beach fetch distance and aeolian sediment transport. *Sedimentology*, 46, 517–522.
Jackson, J.A., 2003. *Glossary of Geology*, 4th edition. Berlin: Springer, 769p.
King, C.A.M. and Williams, W.E., 1949. The formation and movement of sand bars by wave action. *Geographical Journal*, 113, 70–85.
Kirby, R., 2000. Practical implications of tidal flat shape. *Continental Shelf Research*, 20, 1061–1077.
Krinsley, D.H. and Donahue J., 1968. Environmental interpretation of sand grain surface textures by electron microscopy. *Geological Society of America Bulletin*, 79, 743–748.
Krinsley, D.H. and Doornkamp J.C., 1973. *Atlas of Quartz Sand Surface Textures*. Cambridge: Cambridge University Press, 91p.
Kroon, A. and Masselink, G., 2002. Morphodynamics of intertidal bar morphology on a macrotidal beach under low-energy wave conditions, North Lincolnshire, England. *Marine Geology*, 190, 591–608. doi:10.1016/S0025-3227(02)00475-9
Krumbein, W.C., 1934. Size Frequency Distribution of Sediments. *Journal of Sedimentary Petrology*, 4, 65–77.
Latapy, A.; Héquette, A.; Nicolle, N., and Pouvreau, N., 2020. Assessing the influence of changes in shoreface morphology since the 19th century on nearshore hydrodynamics and shoreline evolution in northern France: A modeling approach. *In:* Malvárez, G. and, Navas, F. (eds.), *Global Coastal Issues of 2020*. *Journal of Coastal Research*, Special Issue No. 95, pp. 542–547.
Le Hir, P.; Roberts, W.; Cazaillet, O.; Christie, M.; Bassoullet, P., and Bacher, G., 2000. Characterization of intertidal flat hydrodynamics. *Continental Shelf Research*, 20, 1433–1459.
Le Ribault, L., 1977. *L'exoscopie des quartz*. Paris: Masson, 150p.
McKindsey, C.W.; Archambault P.; Callier, M.D., and Olivier, F., 2011. Influence of suspended and off-bottom mussel culture on the sea bottom and benthic habitats: A review. *Canadian Journal of Zoology*, 89(7), 622–646. doi:10.1139/z11-037
Mahaney, F., 2002. *Atlas of Sand Grain Surface Textures and Applications*. Oxford: Oxford University Press, 237p.
Malvarez, G.; Navas, F., and Jackson, D.W.T., 2004. Investigations on the morphodynamics of sandy tidal flats: A modeling application. *Coastal Engineering*, 51, 731–747.

Margolis, S., 1968. Electron microscopy of chemical solution and mechanical abrasion features on quartz sand grains. *Sedimentary Geology*, 2, 243–256.

Maspataud, A., 2011. Impacts des tempêtes sur la morphodynamique du profil côtier en milieu macrotidal. Dunkerque, France: Université du Littoral-Côte d'Opale, Thèse de doctorat, 516p. (published online, HAL).

METEO France, 2023. *METEO France*. https://meteofrance.com

Pezerat, M.; Bertin, X.; Martins, K.; Mengual, B., and Hamm, L., 2021. Simulating storm waves in the nearshore area using spectral model: Current issues and a pragmatic solution? *Ocean Modelling*, 158, 101737. doi:10.1016/j.ocemod.2020.101737

Reichmüth, B. and Anthony, E.J., 2008. Dynamics of intertidal drainage channels on a multi-barred macrotidal beach. *Earth Surface Processes and Landforms*, 33, 142–151. doi:10.1127/0372-8854/2008/0052S3-0079

Reineck, H.E. and Singh, I.B., 1980. *Depositional Sedimentary Environments*. Berlin: Springer, 549p.

ROLNP (Réseau d'Observation du Littoral de Normandie et des Hauts de France), 2020. *ROLNP*. https://www.rolnp.fr

Ruz, M.-H.; Héquette, A.; Marin, D.; Sipka, V.; Crapoulet, A., and Cartier, A., 2017. Development of an incipient foredune field along a prograding macrotidal shoreline, northern France. *Géomorphologie—relief*, *processus*, *environnement*, 23(1), 37–50. doi:10.4000/geomorphologie.11638

Ruz, M.H. and Meur-Férec, C., 2004. Influence of high-water levels on aeolian sand transport: Upper beach/dune evolution on a macrotidal coast, Wissant Bay, northern France. *Geomorphology*, 60(1–2), 73–87.

Sedrati, M. and Anthony, E.J., 2007. Storm-generated morphologic change and longshore sand transport in the intertidal zone of a multi-barred macrotidal beach. *Marine Geology*, 244, 201–229.

Sharp, R., 1963. Wind ripples. *The Journal of Geology*, 71(5), 617–636.

Short, A.D., 1999. Wave-dominated beaches. *In:* Short, A.D. (ed.), *Handbook of Beach and Shoreface Morphodynamics*. Chichester, U.K.: Wiley, pp. 173–203.

Sipka, V. and Anthony, E.J., 1999. Morphology and hydrodynamics of a macrotidal ridge and runnel beach under modal low wave conditions. *Journal de Recherche Océanographique*, 24, 25–31.

Stevic, M., 2015. Identification and Environmental Interpretation of Microtextures on Quartz Grains from Aeolian Sediments—Brattforsheden and Vittskövle, Sweden. Lund, Sweden: Lund University, Bachelor's thesis, 35p.

Tessier, B.; Corbau, C.; Chamley, H., and Auffret, J-P. 1999. Internal structure of shoreface banks revealed by high-resolution seismic reflection in a macrotidal environment (Dunkerque Area, Northern France). *Journal of Coastal Research*, 15(3), 593–606.

Trefethen, J.M. and Dow, R.L., 1960. Some features of modern beach sediments. *Journal of Sedimentary Petrology*, 30(4), 589–602.

Tresca, A., 2013. Contrôle souple de la dynamique éolienne sur un littoral artificialisé et propositions de gestion: Le cas de la façade maritime du Grand Port Maritime de Dunkerque. Dunkerque, France: Université du Littoral-Côte d'Opale, Thèse de doctorat, 397p. (published online, HAL).

Vanhée, S.; Anthony, E., and Ruz, M.H., 2002. Aeolian sand transport on a ridge and runnel beach: Preliminary results from Leffrinckoucke Beach, northern France. *In:* Cooper, J.A.G. and, Jackson, D.W.T. (eds.), *The 7th International Coastal Symposium (ICS 2002)*. *Journal of Coastal Research*, Special Issue No. 36, pp. 732–740.

Vos, K.; Vandenberghe, N., and Elsen, J., 2014. Surface textural analysis of quartz grains by scanning electron microscopy (SEM): From sample preparation to environmental interpretation. *Earth Sciences Reviews*, 128, 93–104.

Wang, Y.; Wang, Y.; Yu, Q.; Du, Z.; Wang, Z., and Gao, S., 2019. Sand-mud tidal flat morphodynamics influenced by alongshore tidal currents. *Journal of Geophysical Research-Oceans*, 124(6), 3818–3836. doi:10.1029/2018JC014550

Wright, L.D. and Short, A.D., 1984. Morphodynamic variability of beaches and surf zones, a synthesis. *Marine Geology*, 56, 92–118.

Zemmour, A., 2019. Etude de l'évolution des littoraux dunaires de la Côte d'Opale à différentes échelles de temps: Analyse de leur capacité de régénération post-tempête. Dunkerque, France: Université du Littoral-Côte d'Opale, Thèse de doctorat, 270p. (published online, HAL).